Article

Cancer Cell

Regulation of OGT by URI in Response to Glucose Confers c-MYC-Dependent Survival Mechanisms

Graphical Abstract

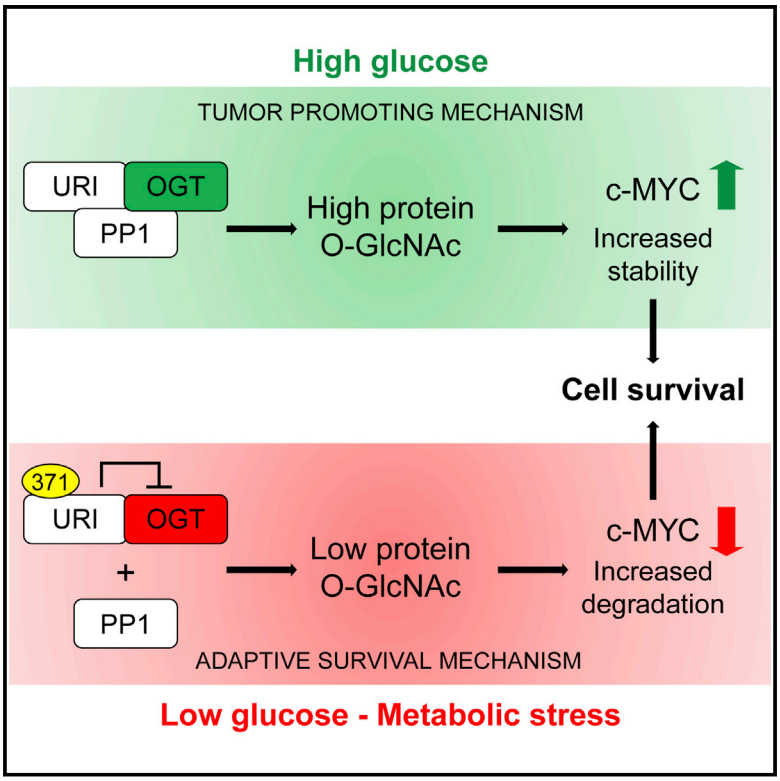

Highlights

- URI/OGT/PP1γ forms a functional heterotrimeric complex in cancer cells
- Glucose depletion phosphorylates URI at Ser-371, releasing PP1γ to inhibit OGT
- OGT inhibition reduces c-MYC, promoting cancer cell survival upon metabolic stress
- URI (S371A) increases O-GlcNAcylation, c-MYC levels, and hepatocarcinogenesis

Authors

Stefan Burén, Ana L. Gomes, Ana Teijeiro, ..., Ramón Campos-Olivas, Diego Megías, Nabil Djouder

Correspondence

ndjouder@cnio.es

In Brief

Burén et al. show that glucose maintains a heterotrimeric URI/OGT/PP1γ complex and reveal a glucose-sensing mechanism in which URI acts as a rheostat regulating OGT, the enzyme catalyzing O-GlcNAcylation and thereby impacting c-MYC stability. Activated OGT and c-MYC stabilization accelerate hepatocarcinogenesis.

Burén et al., 2016, Cancer Cell *30*, 290–307
August 8, 2016
http://dx.doi.org/10.1016/j.ccell.2016.06.023

CellPress

CellPress

Cancer Cell
Article

Regulation of OGT by URI in Response to Glucose Confers c-MYC-Dependent Survival Mechanisms

Stefan Burén,[1] Ana L. Gomes,[1] Ana Teijeiro,[1] Mohamad-Ali Fawal,[1] Mahmut Yilmaz,[1] Krishna S. Tummala,[1] Manuel Perez,[2] Manuel Rodriguez-Justo,[3] Ramón Campos-Olivas,[4] Diego Megías,[2] and Nabil Djouder[1,*]

[1]Cancer Cell Biology Programme, Growth Factors, Nutrients and Cancer Group
[2]Biotechnology Programme, Confocal Microscopy Core Unit
Centro Nacional de Investigaciones Oncológicas, CNIO, Madrid 28029, Spain
[3]Department of Research Pathology, Cancer Institute, University College London, London WC1E 6JJ, UK
[4]Structural Biology and Biocomputing Programme, Spectroscopy and Nuclear Magnetic Resonance Unit, Centro Nacional de Investigaciones Oncológicas, CNIO, Madrid 28029, Spain
*Correspondence: ndjouder@cnio.es
http://dx.doi.org/10.1016/j.ccell.2016.06.023

SUMMARY

Cancer cells can adapt and survive under low nutrient conditions, but underlying mechanisms remain poorly explored. We demonstrate here that glucose maintains a functional complex between the co-chaperone URI, PP1γ, and OGT, the enzyme catalyzing O-GlcNAcylation. Glucose deprivation induces the activation of PKA, which phosphorylates URI at Ser-371, resulting in PP1γ release and URI-mediated OGT inhibition. Low OGT activity reduces O-GlcNAcylation and promotes c-MYC degradation to maintain cell survival. In the presence of glucose, PP1γ-bound URI increases OGT and c-MYC levels. Accordingly, mice expressing non-phosphorylatable URI (S371A) in hepatocytes exhibit high OGT activity and c-MYC stabilization, accelerating liver tumorigenesis in agreement with c-MYC oncogenic functions. Our work uncovers that URI-regulated OGT confers c-MYC-dependent survival functions in response to glucose fluctuations.

INTRODUCTION

Glucose deficiency causes metabolic stress, cell dysfunction, and eventual death. Sophisticated (but not well understood) mechanisms have evolved that activate protective functions under metabolic challenge, allowing cancer cells to survive independently of nutrient availability (Ma et al., 2013). Whereas most cellular glucose is metabolized during glycolysis, some is converted via the hexosamine biosynthetic pathway, leading to formation of the acetylated amino sugar nucleotide uridine diphosphate N-acetylglucosamine (UDP-GlcNAc). UDP-GlcNAc is the donor in O-GlcNAcylation, a glucose-dependent post-translational modification (Hardiville and Hart, 2014), dynamically attached to serine or threonine protein residues, thus representing an alternative to phosphorylation to modulate protein behavior and cell signaling.

O-GlcNAcylation levels changes in response to cellular glucose concentrations. While many enzymes catalyze protein phosphorylation and dephosphorylation, O-GlcNAcylation is catalyzed by a single O-linked N-acetylglucosamine transferase (OGT). Removal of protein-linked O-GlcNAc is performed by another single enzyme, β-N-acetylglucosaminidase (O-GlcNAcase or OGA). OGT integrates changes in glucose concentrations and transfers the information to downstream effectors, thus controlling diverse cellular processes (Hardiville and Hart, 2014). OGT's substrate diversity suggests that its localization and activity are modulated by partner binding.

Increased O-GlcNAcylation is observed in various tumors (Caldwell et al., 2010; Ferrer et al., 2014; Ma and Vosseller, 2014; Slawson et al., 2010; Zhu et al., 2012, 2016), but its contribution to tumorigenesis is not well understood. Identification of

Significance

Increased O-GlcNAcylation is observed in cancer cells, but its contribution to tumorigenesis is poorly understood. Using various cancer cell lines, we demonstrate that under glucose-limited conditions, phosphorylated URI releases PP1γ and inhibits OGT, thereby enhancing c-MYC turnover to provide survival mechanisms. When glucose is abundant, non-phosphorylated URI that is bound to PP1γ activates OGT, thereby increasing c-MYC levels. Activated OGT and enhanced c-MYC are shown to promote hepatocarcinogenesis, while a c-MYC inhibitor (JQ1) mitigates HCC. Our findings delineate a glucose-sensing mechanism in which URI acts as a rheostat regulating OGT activity and c-MYC levels, triggering adaptive responses that enable mammalian cells to survive under pathological low glucose. This may occur in poorly vascularized tumors, leading to glucose deficiency.

specific OGT binding partners and understanding their regulation in response to metabolic stress should clarify how O-GlcNAcylation modulates cellular responses and how fluctuations in glucose levels activate survival mechanisms, especially important in maintaining tumor growth during periods of metabolic stress, and thus elucidate how O-GlcNAcylation contributes to tumorigenesis.

A functional complex comprising OGT and the protein phosphatase 1γ (PP1γ) catalytic subunit has been reported (Wells et al., 2004). Additionally, the co-chaperone unconventional prefoldin RPB5 interactor (URI) has been shown to regulate PP1γ activity (Djouder et al., 2007). URI has also oncogenic activities, and its expression in murine hepatocytes induces spontaneous hepatocellular carcinoma (HCC) (Tummala et al., 2014). Therefore, we investigate the role of the trimeric complex formed by URI, OGT, and PP1γ in regulating cellular O-GlcNAcylation in response to metabolic stress and its function in tumorigenesis, such as HCC development.

RESULTS

URI, OGT, and PP1γ Form a Heterotrimeric Complex

Hypothesizing that URI, OGT, and PP1γ form a functional complex, we first investigated interactions between OGT and URI in various cancer cell lines, such as human embryonic kidney (HEK)-293T and human osteosarcoma U2OS cells. In this study, we additionally validated our mechanism in different HCC cells (Huh7, HepG2, SNU398, and SNU449). Both URI and PP1γ co-purified with OGT, but OGT suppression (siOGT) attenuated their interactions in HEK293T cells (Figures 1A and 1B). Overexpressed hemagglutinin (HA)-tagged OGT (HA-OGT) interacted with endogenous URI (Figures S1A–S1D). Reciprocally, endogenous OGT immunoprecipitated with HA-URI (Figures S1E and S1F). Furthermore, OGT, URI, and PP1γ co-eluted in high molecular weight fractions in gel filtration (Figure S1G). Mitochondria purification and co-immunoprecipitation (coIP) assays in U2OS cells suggested that URI/OGT/PP1γ can form a mitochondrial complex (Figures S1H and S1I) (Djouder et al., 2007; Love et al., 2003).

Next, direct OGT binding to URI was tested. Recombinant glutathione S-transferase (GST) or GST-tagged OGT were incubated with in vitro translated (IVT) full-length (FL) HA-URI or different HA-URI fragments. Pulldowns revealed that URI's N-terminal (Nt) part (residues 1–193) interacted with OGT (Figures 1C and 1D). OGT binding to PP1γ was confirmed by incubating GST-OGT with IVT HA-PP1γ (Figures S1J and S1K).

PP1γ binds to a different, C-terminal (Ct) part of URI (Djouder et al., 2007), so OGT, PP1γ, and URI can form a single complex (Figure 1E). PP1γ interaction with URI in OGT-depleted HEK293T cells was reduced, suggesting that OGT is important for PP1γ binding to URI (Figures 1F and 1G). Additionally, URI/PP1γ interaction was strengthened by the non-phosphorylatable S371A point mutation of URI (Djouder et al., 2007). PP1γ immunoprecipitates also revealed greater binding of PP1γ to OGT in HEK293T cells overexpressing HA-URI (S371A) than in cells expressing HA-URI (WT) (wild-type) (Figures S1L and S1M). Finally, binding of IVT HA-PP1γ to GST-OGT was enhanced when His-tagged URI (His-URI) was added in a dose-dependent manner (Figures 1H–1J), suggesting a heterotrimeric URI/OGT/PP1γ complex.

URI binds the Ct region of PP1γ (245–323) in vitro (Figures S1N and S1O), which contains a hydrophobic pocket for regulatory proteins (Bollen et al., 2010). Mutating residues of the PP1γ hydrophobic groove (Gibbons et al., 2005) disrupted PP1γ/URI interaction (Figures S1P–S1R), confirming that URI regulates PP1γ (Djouder et al., 2007). IVT HA-OGT (FL) bound equally the different GST-PP1γ versions (Figures S1S–S1U), suggesting that OGT and URI bind to different PP1γ sites.

OGT consists of a series of Nt tetratricopeptide repeats (TPR, critical for target protein recognition) and a Ct enzymatic domain (ED, the glycosyltransferase subunit) (Lazarus et al., 2011). Overexpression of Myc-tagged OGT (FL) and OGT fragments containing the TPR motif or ED in HEK293T cells revealed that URI preferentially binds to the ED (Figures 1K–1N).

URI Inhibits OGT Activity In Vitro and In Vivo

Hypothesizing (from URI's binding to the OGT ED) that URI regulates OGT's glycosyltransferase activity, we determined by immunofluorescence O-GlcNAc levels in URI- or OGT-depleted U2OS cells, which respectively increased and abolished O-GlcNAc signals (Figures 2A and 2B). Dot blots and western blotting (WB) against O-GlcNAc using several URI small interfering RNAs (siRNAs) confirmed these results (Figures 2C, 2D, S2A, and S2B). OGA levels remained constant upon URI depletion but decreased in OGT-depleted cells, possibly to maintain O-GlcNAcylation homeostasis (Figure S2A) (Zhang et al., 2014). Conversely, URI overexpression reduced O-GlcNAcylation (Figures 2E, 2F, S2C, and S2D). Importantly, the O-GlcNAc antibodies' specificity (CTD110.6 versus 1F5.D6(14) clones) confirmed that CTD110.6 is highly specific, and dot blots provided sensitive and quantitative assessments of O-GlcNAc differences (Figures S2E–S2K). Thus, URI may inhibit OGT catalytic activity.

To test whether URI directly inhibits OGT, potentially via binding to the ED, we established an in vitro OGT activity assay using recombinant OGT and non-glycosylated TAK1-binding (TAB1) protein (Pathak et al., 2012). Treatment with recombinant GST-URI caused a slight dose-dependent reduction in TAB1 O-GlcNAcylation (Figures S2L–S2N). Because URI interacts with OGT via its Nt domain (Figures 1C–1E), the bulky Nt GST tag could affect OGT inhibition efficiency. URI with a smaller tag (His-URI) pulled down recombinant OGT using Ni-nitrilotriacetic acid (NTA) beads (Figures 2G, S2O, and S2P) or a URI antibody (Figure S2Q). His-URI caused drastic dose-dependent inhibition of OGT activity toward TAB1 (Figures 2H and 2I). Thus, URI inhibits OGT-mediated O-GlcNAcylation.

Protein Kinase A Phosphorylates URI at Ser-371 upon Glucose Deprivation

URI may regulate OGT activity in response to abnormal glucose levels. An antibody was generated (Figures S3A–S3D and Experimental Procedures) to investigate the effects of glucose deprivation-induced metabolic stress on URI phosphorylation at Ser-371, which regulates PP1γ activity (Djouder et al., 2007). Unless specified, glucose-deprived cells were first serum-starved overnight (in the presence of glucose), then glucose was withdrawn for the indicated time. Ser-371 phosphorylation was detected within 30 min of glucose deprivation in U2OS cells and strengthened after 2 hr (Figure 3A). URI knockdown and λ-phosphatase (λPPase) confirmed Ser-371 signal specificity (Figures

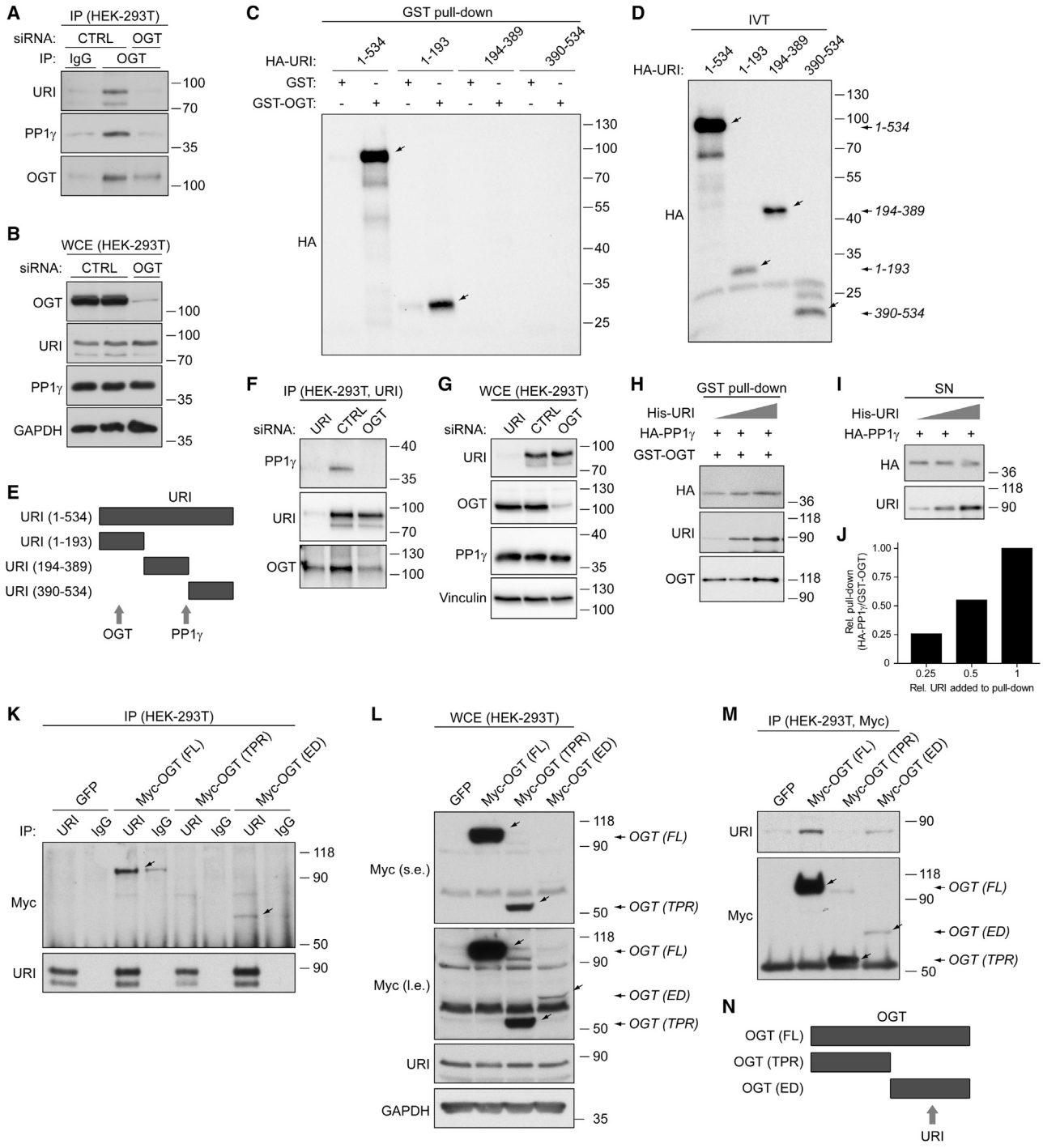

Figure 1. URI, OGT, and PP1γ Form a Heterotrimeric Complex

(A and B) CoIP (A) of URI and PP1γ with OGT in siRNA-transfected HEK-293T whole-cell extracts (WCE) (B).

(C and D) Pulldown (C) of IVT FL HA-URI (1–534) and HA-URI fragments (D) using GST or GST-OGT. Arrows indicate FL HA-URI and HA-URI fragments.

(E) Scheme depicting binding of OGT and PP1γ to URI.

(F and G) CoIP (F) of OGT and PP1γ with URI in siRNA-transfected HEK-293T WCE (G).

(H–J) Pulldown (H) and supernatant (SN) (I) of IVT HA-PP1γ with His-URI using GST-OGT. Quantification (J) of HA-PP1γ/GST-OGT ratios calculated from (H).

(K–M) WCE from HEK-293T transiently expressing GFP, Myc-tagged FL OGT, or Myc-tagged OGT fragments (corresponding to the TPR region [TPR] or enzymatic domain [ED]) (L) were used for coIP using URI (K) or Myc (M) antibodies. Short (s.e.) and long (l.e.) exposures are indicated. Arrows indicate Myc-tagged OGT and OGT fragments.

(N) Scheme indicating URI binding to OGT as observed from (K) and (M).

See also Figure S1.

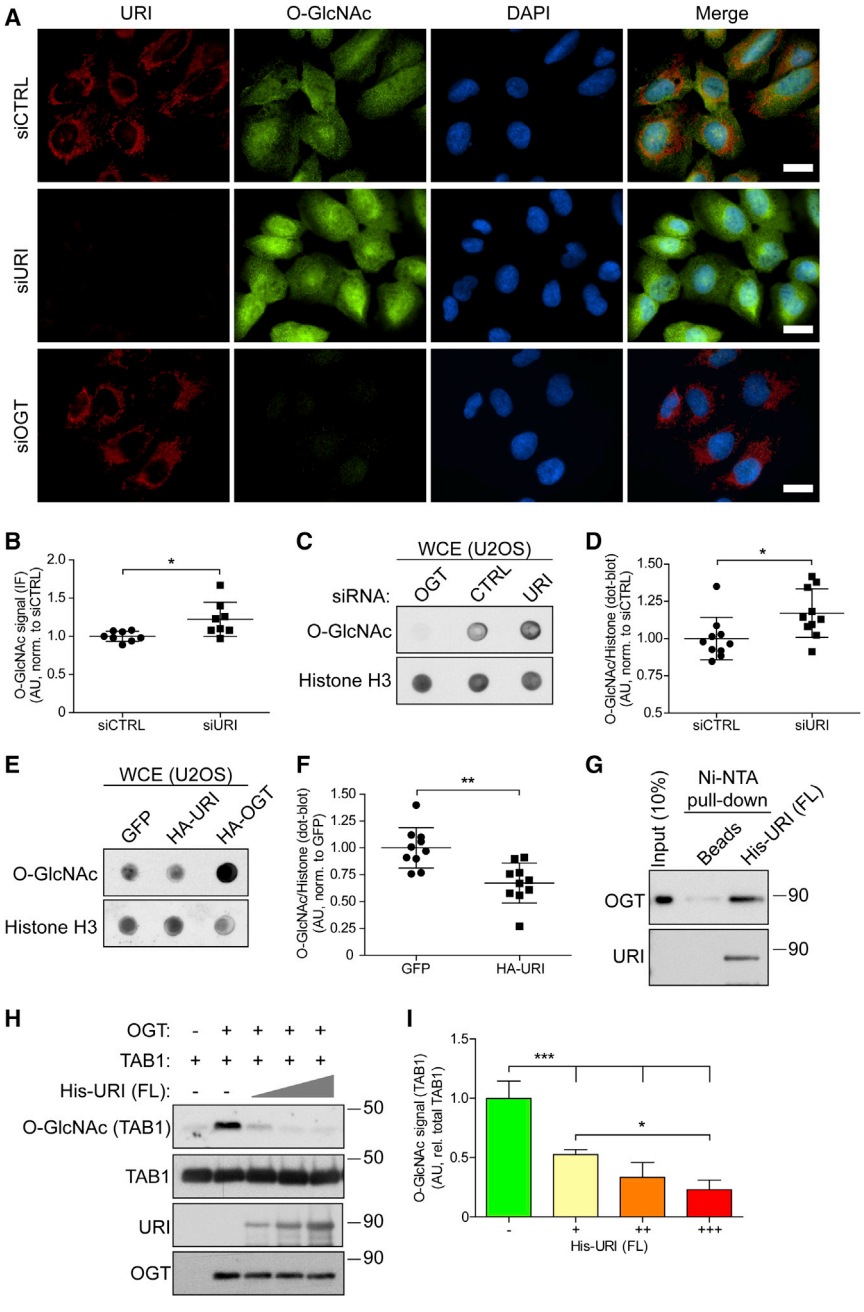

Figure 2. URI Inhibits OGT Activity In Vitro and In Vivo

(A and B) Immunofluorescence (A) and quantification of O-GlcNAc signal intensity per cell (B) in siRNA-transfected U2OS cells. n = 8 (average of ≥4 fields per experiment). Scale bar, 20 μm.

(C and D) Dot blots (C) and quantification of O-GlcNAc signals (D) in siRNA-transfected U2OS cells (Figure S2A). n = 10.

(E and F) Dot blots (E) and quantification of O-GlcNAc signals (F) in plasmid-transfected U2OS cells (Figure S2D). n = 10.

(G) Ni-NTA pulldown of recombinant OGT in the absence or the presence of FL His-URI.

(H and I) In vitro O-GlcNAcylation (H) and quantification (I) of TAB1 using recombinant OGT in the absence or the presence of FL His-URI. n = 5.

For (B), (D), (F), and (I), mean and SD error bars are shown. *p < 0.05, **p < 0.01, ***p < 0.001, unpaired t test (B, D, and F) or one-way ANOVA (p < 0.0001) followed by Tukey's multiple-comparison post test (I).

See also Figure S2.

S3E and S3F). Notably, Ser-371 phosphorylation was independent of the mammalian/mechanistic target of rapamycin (mTOR)/S6K1 axis (Figures S3G and S3H). Finally, glucose derivation in cells cultured in varying concentrations of dialyzed serum did not affect Ser-371 phosphorylation (Figure S3I). Thus, glucose depletion results in URI phosphorylation specifically at Ser-371.

To identify kinase(s) that may phosphorylate Ser-371 following glucose depletion, we constructed URI Ser-371 fluorescence resonance energy transfer (FRET) probes (Figures 3B, S3J, and S3K). One, based on URI amino acids 343–375 (URI2; Figure 3B), generated enhanced FRET in glucose-deprived U2OS cells (Figure 3C). Because Thr-349 represents another potential phosphorylation site, we confirmed that FRET required Ser-371 phosphorylation using an S371A variant (Figures 3C, S3L, and S3M).

As Ser-371 is located in the AGC kinase consensus motif ($^{R}/_{K}KX^{S}/_{T}$), we downregulated 58 AGC kinases using siRNAs in U2OS cells and monitored Ser-371 phosphorylation by WB and FRET. Few kinases, including protein kinase A (PKA) α/β/γ isoforms, contributed to Ser-371 phosphorylation following glucose deprivation (Figures 3D, S3N, and S3O). PKA activation reduces O-GlcNAcylation, and can form a functional mitochondrial holoenzyme complex with PP1 (Danial et al., 2003; Griffith and Schmitz, 1999). We therefore hypothesized that PKA links low glucose to URI-mediated OGT regulation.

Using additional PKAα, β, and γ isoform siRNAs, reduced URI Ser-371 phosphorylation was confirmed. Notably, PKAα most efficiently phosphorylated URI Ser-371 (Figure 3E). Furthermore, recombinant PKA phosphorylated GST-URI (WT) in vitro on Ser-371, but not GST-URI (S371A). Addition of PKA inhibitor abolished Ser-371 phosphorylation (Figure 3F). Ser-371 is thus a genuine PKA phosphorylation site in vitro. Ser-371 phosphorylation also occurred when U2OS cells were serum deprived and treated with forskolin (FSK), a cAMP booster and PKA activator (Figure 3G). Additionally, several HCC cell lines and U2OS were glucose deprived while PKA was inhibited using H89 or cell-permeable myristoylated PKA inhibitor peptide. Glucose deprivation-induced URI phosphorylation at Ser-371 was PKA inhibitor sensitive in U2OS, Huh7, and HepG2 cells. Glucose withdrawal in SNU449 cells did not further increase

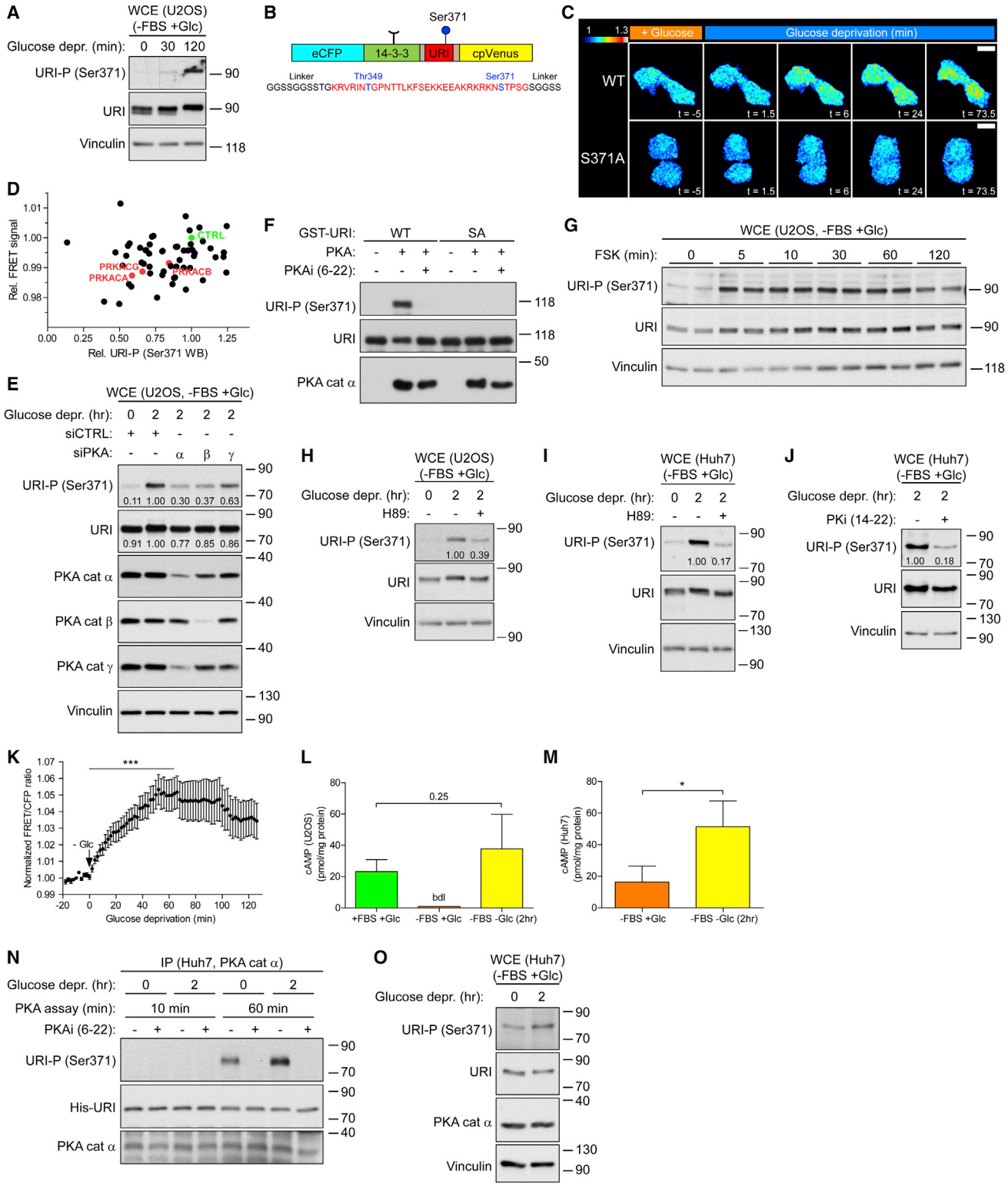

Figure 3. PKA Phosphorylates URI at Ser-371 upon Glucose Deprivation

(A) WB of U2OS WCE in response to glucose deprivation.

(B) Graphic illustration of the URI FRET probe. Amino acids corresponding to URI 343-375 are highlighted in red.

(C) FRET induction in URI FRET probes ((WT) and (S371A)) in U2OS cells upon glucose deprivation. Scale bar, 20 μm.

(legend continued on next page)

URI phosphorylation at Ser-371 but was completely abolished by H89, suggesting that SNU449 cells may have a sustained PKA activity (Figures 3H–3J and S3P–S3R). Furthermore, PKA FRET signal increased upon glucose depletion in U2OS cells, indicating that glucose withdrawal stimulates PKA (Figure 3K) (Allen and Zhang, 2006). Importantly, cyclic AMP (cAMP) levels were elevated in glucose-deprived U2OS and Huh7 cells, but did not change in SNU449 cells (Figures 3L, 3M, and S3S). Finally, immunoprecipitated PKA from glucose-starved Huh7 cells phosphorylated URI at Ser-371 in vitro (Figures 3N and 3O). Thus, glucose depletion induces a cAMP-dependent PKA activation, which phosphorylates URI at Ser-371.

Glucose Deprivation Maintains ATP Pools and Induces a cAMP-Dependent PKA Activation

Although ATP levels were reduced in glucose-depleted cells (Figure 4A), they might be sufficient to generate cAMP (see Figures 3L and 3M). URI phosphorylation was therefore monitored by treating cells with inhibitors of metabolic pathways that can be affected by glucose depletion. Rapamycin (mTOR inhibitor) slightly decreased URI phosphorylation, while *trans*-androsterone (pentose phosphate pathway inhibitor) and rotenone (mitochondria electron transport chain inhibitor) showed no decrease (Figure 4B). However, rotenone treatment for 2 hr at 1 μM (Doege et al., 2005) neither abolished ATP production (not shown) nor induced AMP kinase (AMPK) activation (Figure 4B). Addition of 2-deoxy-D-glucose (2DG), a glucose analog that cannot be metabolized through glycolysis and which affects ATP levels (Wick et al., 1957), activated AMPK and abolished URI phosphorylation at Ser-371 (Figure 4B), suggesting that decreased energy, and thus ATP production, may inhibit cAMP-induced PKA activation. Glucose deprivation in U2OS cells pretreated with higher rotenone concentration (2 μM) for a longer period of time (16 hr) lowered ATP levels, activated AMPK phosphorylation at Thr-172, and significantly reduced cAMP and URI Ser-371 phosphorylation (Figures 4C, 4D, and S4A). The ATP/cAMP axis may thus be required for PKA activation-mediated URI phosphorylation.

Effects from rotenone suggested that oxidative phosphorylation may still generate ATP during short-term glucose starvation. To explore metabolic pathways that might be affected by glucose deprivation, we used nuclear magnetic resonance (NMR) to analyze partitioning of [^{13}C]glucose and to detect several metabolites in U2OS cells (Figure S4B). Glucose depletion over 2 hr reduced glutamate and threonine concentrations (Figures 4E and 4F) while, independently of URI and OGT knockdown, several amino acids of the tricarboxylic acid (TCA) cycle accumulated, especially aspartate, which potentially originated from transamination of oxaloacetate (Figures 4G and S4C–S4J), suggesting that glucose depletion induces anaplerosis to replenish TCA-cycle intermediates, maintaining ATP pools and, thus, cAMP-PKA activation (Figure 4H).

Glucose Depletion-Induced PP1γ Release Promotes URI-Mediated OGT Inhibition

Next, we investigated the responses of the URI/PP1γ/OGT complex to glucose depletion. PP1γ immunoprecipitation revealed a glucose depletion time-dependent reduction in PP1γ-associated URI, accompanied by Ser-371 phosphorylation that inversely correlated with O-GlcNAcylation levels in U2OS and HEK293T cells (Figures 5A, 5B, and S5A–S5C). URI/PP1γ complex dissociation and URI phosphorylation were pronounced upon 2 hr of glucose deprivation. Adding FSK significantly reduced URI/PP1γ complex formation (Figures 5C–5E).

Expectedly, H89-mediated PKA inhibition increased URI/PP1γ complexes in glucose-deprived Huh7 cells (Figures S5D and S5E). Similarly, glucose withdrawal in U2OS and Huh7 cells overexpressing URI (S371A) mutant did not affect URI/PP1γ/OGT interaction but rather increased it (Figures 5F, 5G, S5F, and S5G). Importantly, interaction between URI and PP1γ was lost in Huh7 cells expressing the phospho-mimicking HA-URI (S371D) mutant (Figures 5H and S5H). Adding glucose to glucose-deprived U2OS cells reduced Ser-371 phosphorylation but did not completely restore URI/PP1γ binding (Figures S5I and S5J), suggesting that glucose is not sufficient to fully restore this interaction.

Glucose deprivation or FSK-mediated PKA activation reduced O-GlcNAc contents in U2OS and Huh7 cells, while OGT and OGA levels were not affected (Figures 5B, S5E, and S5K). In glucose-deprived cells treated with PKA inhibitor or overexpressing HA-URI (S371A), O-GlcNAc levels were enhanced compared with non-treated cells or cells overexpressing HA-URI (WT) (Figures 5I, S5E and S5L). Importantly, O-GlcNAcylation was dramatically reduced in Huh7 and HepG2 cells overexpressing HA-URI (S371D) compared with HA-URI (WT) (Figures 5I–5L and S5L). Thus, in glucose-depleted

(D) Scatterplot of URI Ser-371 phosphorylation upon 2 hr of glucose deprivation (URI FRET signal plotted against URI-P(Ser371) WB signal [Figure S3N]) in U2OS cells transfected with siRNAs against AGC kinases. siCTRL (green dot) and siRNA against PKA catalytic subunits (siPKAs cat α, β, and γ) (red dots) transfected cells are highlighted.

(E) WB of U2OS cells transfected with PKA targeting siRNAs (unique siRNAs from those used in AGC kinase screen [Figures S3N and S3O]). Notably, PKA cat γ antibody cross-reacts with PKA cat α subunit.

(F) In vitro kinase assay in the absence or the presence of PKA inhibitor fragment 6–22 (PKAi, 2 μM).

(G) WB of U2OS cells treated with forskolin (FSK, 20 μM).

(H–J) WB analysis of U2OS (H) and Huh7 (I and J) cells treated with PKA inhibitor H89 (10 μM) (H and I) or PKA inhibitor fragment 14–22 (PKi, 100 μM) (J) in response to glucose deprivation.

(K) PKA activity, measured as FRET ratio normalized to FRET levels prior to glucose deprivation, in U2OS cells expressing PKA sensor. n = 10.

(L) cAMP levels in U2OS cells. n = 4 (+FBS +Glc), n = 3 (−FBS +Glc), and n = 5 (−FBS −Glc). bdl, below detection limit.

(M) cAMP levels in Huh7 cells. n = 4.

(N and O) In vitro kinase assay of His-URI (N) using PKA immunoprecipitated from glucose-depleted Huh7 cells (O), in the absence or the presence of PKA inhibitor fragment 6–22 (PKAi, 2 μM).

For (K–M), mean and SEM (K) or SD (L and M) error bars are shown. *$p < 0.05$, ***$p < 0.001$, unpaired t test.

See also Figure S3.

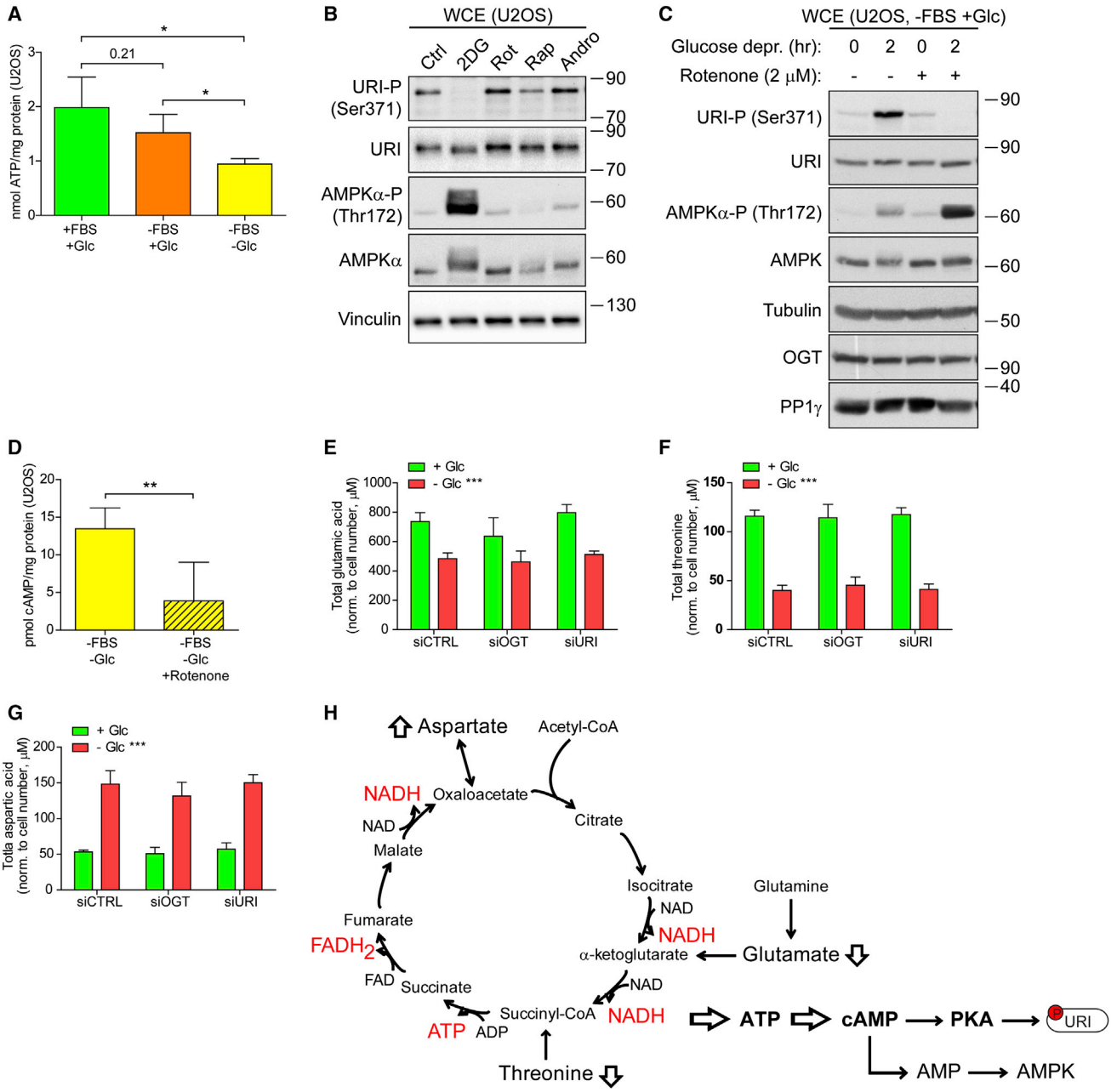

Figure 4. Glucose Deprivation Maintains ATP Pools and Induces cAMP-Dependent PKA Activation

(A) ATP levels in U2OS cells. n = 4.

(B) WB of U2OS cells treated with inhibitors (2-deoxy-D-glucose [2DG, 25 mM], rotenone [Rot, 1 μM], rapamycin [Rap, 50 nM], *trans*-androsterone [Andro, 50 μM]) for 2 hr.

(C and D) WB (C) and cAMP quantification (D) of glucose-depleted U2OS cells, in the absence or the presence of rotenone (2 μM). n = 5.

(E–G) Intracellular glutamic acid (E), threonine (F), and aspartic acid (G) levels in siRNA-transfected U2OS cells (Figure S4B). n = 3.

(H) Scheme of how anaplerotic reactions can replenish TCA-cycle intermediates and maintain ATP pools. URI phosphorylated at Ser-371 is indicated with red P letter.

For (A) and (D–G), mean and SD error bars are shown. *p < 0.05, **p < 0.01, ***p < 0.001, unpaired t test (A and D) or two-way ANOVA (E–G).

See also Figure S4.

cells, PKA-phosphorylated Ser-371 disrupts URI/PP1γ complexes and decreases O-GlcNAcylation.

URI/PP1γ complex was also monitored by using inhibitors of metabolic pathways (Figure 4B). Expectedly, 2DG inhibited URI Ser-371 phosphorylation (Figure 4B), strikingly increased URI/PP1γ complex formation, and elevated O-GlcNAcylation in U2OS cells (Figure S5M). Rotenone-mediated cAMP reduction and URI Ser-371 dephosphorylation upon glucose

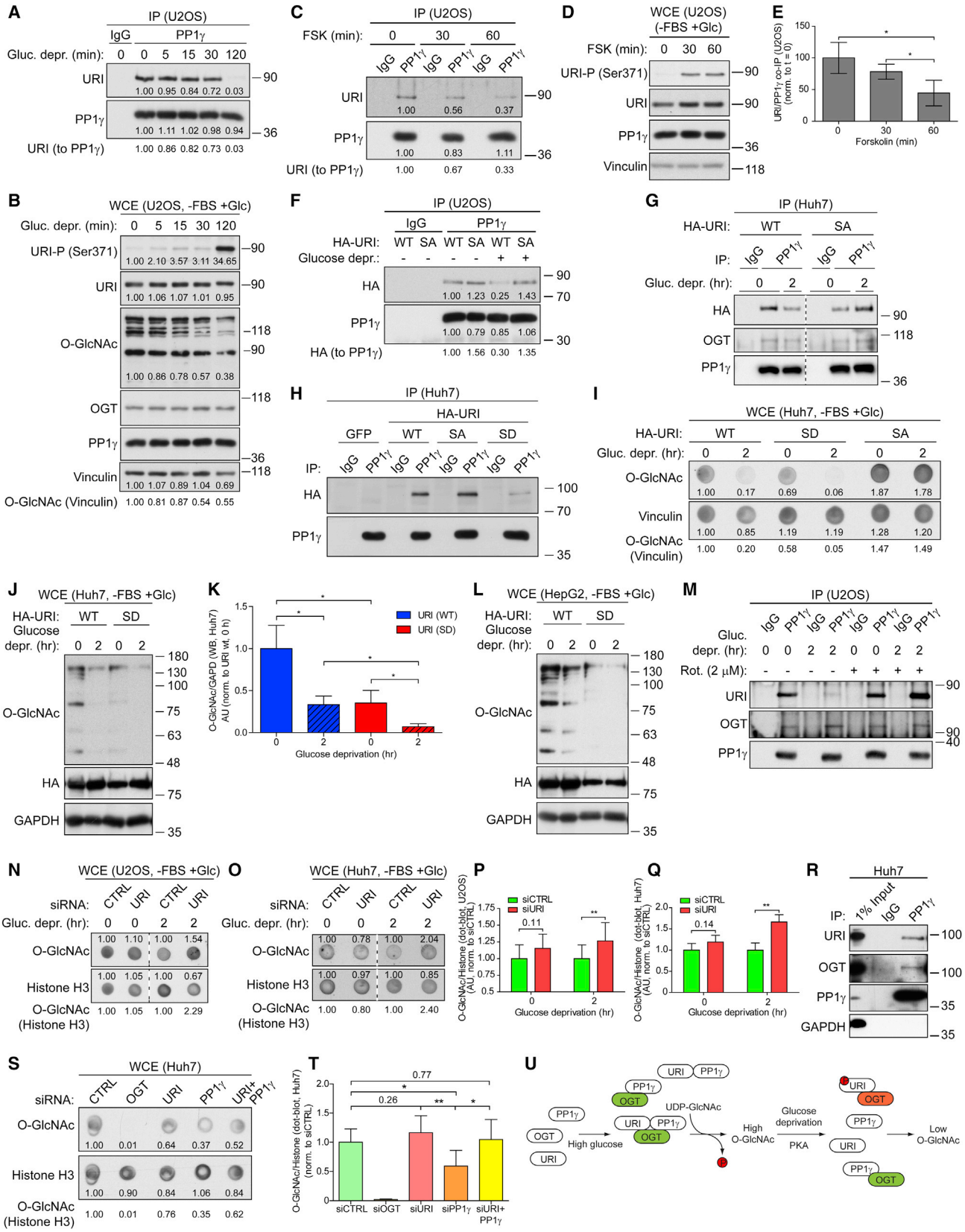

(legend on next page)

deprivation (Figures 4C and 4D) prevented URI/PP1γ dissociation (Figure 5M).

Glucose-deprived U2OS and Huh7 cells treated with URI siRNA had significantly higher O-GlcNAc levels (Figures 5N–5Q and S5N). Glucose deprivation did not affect URI binding to OGT, as seen for PP1γ (Figures S5O–S5Q). Further, pulldowns of GST-OGT and PKA-phosphorylated His-URI showed that phosphorylated and non-phosphorylated URI had similar affinities to GST-OGT (Figure S5R). HA-URI (WT), (S371A), and (S371D) bound GST-OGT to similar extents (Figure S5S), and HA immunoprecipitation in Huh7 cells confirmed that OGT binds equally to the different overexpressed HA-URI versions (Figure S5T). Thus, glucose depletion does not strengthen URI/OGT interaction, but efficient OGT inhibition by URI may require URI Ser-371 phosphorylation and PP1γ release from the heterotrimeric complex.

This hypothesis was tested in various HCC cell lines. PP1γ immunoprecipitated both URI and OGT (Figures 5R and S5U) and glucose deprivation reduced O-GlcNAcylation levels (Figure S5V) in HCC cells. Depletion of PP1γ significantly reduced O-GlcNAcylation in Huh7 and HepG2 cells while URI knockdown restored it in PP1γ-suppressed cells (Figures 5S, 5T, S5W, and S5X). Finally, incubating recombinant OGT with URI and PP1γ (C291R) mutant, which binds OGT but not URI, efficiently reduced in vitro O-GlcNAcylation, compared with PP1γ (WT), which potently binds URI (Figure S5Y). URI thus appears to be a potent OGT inhibitor when free from PP1γ (Figure 5U).

URI Phosphorylation at Ser-371 Protects Cancer Cells from Metabolic Stress-Induced Cell Death

To understand the physiological consequences of URI-mediated OGT inhibition, we analyzed glucose metabolism using the NMR data described above (Figure S4B). In the presence of glucose, URI knockdown increased total glucose uptake and lactate release (Figures S6A–S6D), suggesting that overactive OGT may modulate glycolysis. In the absence of glucose, URI depletion significantly reduced intracellular ^{13}C-labeled glucose levels, suggesting intracellular utilization of remaining glucose, possibly due to overactive OGT (Figure 6A). Thus, URI-mediated OGT inhibition may reduce glucose consumption under glucose restrictions.

To test this, we monitored intracellular glucose levels in U2OS cells expressing an FRET-based glucose sensor (Takanaga et al., 2008). Specificity to glucose was verified by resupplementing glucose-depleted cells with 25 mM glucose, glucosamine, or 2DG (Figure S6E). OGT depletion increased glucose levels, as observed from enhanced FRET signal (Figure 6B), while glucose deprivation in URI-depleted cells significantly reduced FRET signals, corroborating the above NMR data (Figures 6C and 6D).

NMR data indicated that UDP-GlcNAc levels remained unchanged in OGT- or URI-depleted U2OS cells upon glucose deprivation (Figures S6F and S6G), suggesting that OGT inhibition may not affect UDP-GlcNAc pools per se, possibly because they are either too high to be significantly affected by modulation of O-GlcNAcylation, ca. 0.1 to 1 mM (Hart and Akimoto, 2009), or increased glucose uptake that occurs in URI-depleted cells may keep UDP-GlcNAc pools sustained during glucose withdrawal (Figures S6A and S6C). As UDP-GlcNAc levels were similar, glucose utilization is most likely regulated through OGT activity (O-GlcNAc)-regulated targets. Thus, in the presence of glucose, URI depletion (overactive OGT) may increase glucose consumption. Upon glucose limitation, URI knockdown prevents OGT inhibition, possibly resulting in decreased intracellular glucose (as glucose consumption is still high).

These observations suggest that URI knockdown and glucose-depleted cells have lower glucose levels and may therefore be sensitized to apoptosis. URI knockdown decreased U2OS and Huh7 cell number, and increased cell death and O-GlcNAcylation in glucose-depleted conditions (Figures 6E, 6F, and S6H). Overexpression of URI (WT) increased U2OS cell number and cell viability and reduced apoptosis upon glucose removal (Figures 6G and S6I–S6K). Increased cell number was further enhanced in glucose-deprived HCC cells expressing the phospho-mimicking URI (S371D) mutant (Figures 6H and 6I). Overexpression of URI (S371A), which increased O-GlcNAc levels (see Figures 5I and S5L), reduced cell count in glucose-deprived HCC and U2OS cells compared with URI (WT) cells (Figures 6H, 6I, and S6L). In line with previous reports (Djouder et al., 2007; Theurillat et al., 2011), when nutrients are abundant, HCC cells overexpressing URI (S371A), but not URI (S371D), increased cell number (Figures 6J and 6K). OGT inhibition upon URI Ser-371 phosphorylation may thus provide survival signaling specifically

Figure 5. Glucose Depletion-Induced PP1γ Release Promotes URI-Mediated OGT Inhibition

(A–E) CoIP (A and C) of URI with PP1γ in WCE from glucose-deprived (B) or forskolin (FSK)-treated (D) U2OS cells. Quantification of (C) is shown in (E). n = 4.

(F) CoIP of HA-URI (WT and S371A [SA]) with PP1γ in WCE from HA-URI overexpressing U2OS cells (Figure S5F) upon 1 hr of glucose deprivation.

(G) CoIP of HA-URI (WT and SA) with PP1γ in WCE from HA-URI overexpressing Huh7 cells (Figure S5G). Dotted lines indicate sections originating from same membrane, film, and exposure.

(H) CoIP of HA-URI with PP1γ in WCE from GFP or HA-URI (WT, SA, and S371D [SD]) overexpressing Huh7 cells (Figure S5H).

(I) Dot blots and quantification of O-GlcNAc signal in WCE from HA-URI (WT, SD, and SA) overexpressing Huh7 cells.

(J–L) WB (J and L) and quantification (K) of O-GlcNAc signal in WCE from HA-URI (WT and SD) overexpressing Huh7 (J and K) and HepG2 (L) cells. n = 3.

(M) CoIP of URI and OGT with PP1γ in WCE from glucose-depleted U2OS cells (Figure 4C), in the absence or the presence of rotenone (2 μM).

(N–Q) Dot blots (N and O) and quantification (P and Q) of O-GlcNAc signals from siRNA-transfected and glucose-deprived U2OS (N and P) (Figure S5N) and Huh7 (O and Q) cells. Dotted lines indicate different exposures of the same membrane. n = 11 (P) and n = 4 (Q).

(R) CoIP of URI and OGT with PP1γ in Huh7 WCE.

(S and T) Dot blots (S) and quantification (T) of O-GlcNAc signals in WCE from siRNA-transfected Huh7 cells (Figure S5W). n = 7.

(U) Scheme of URI, OGT, and PP1γ interactions in response to glucose deprivation. Active (green) and inhibited (orange) OGT are indicated. URI phosphorylated at Ser-371 is indicated with red P letter.

For (E), (K), (P), (Q), and (T), mean and SD error bars are shown. *$p < 0.05$, **$p < 0.01$, unpaired t test.

See also Figure S5.

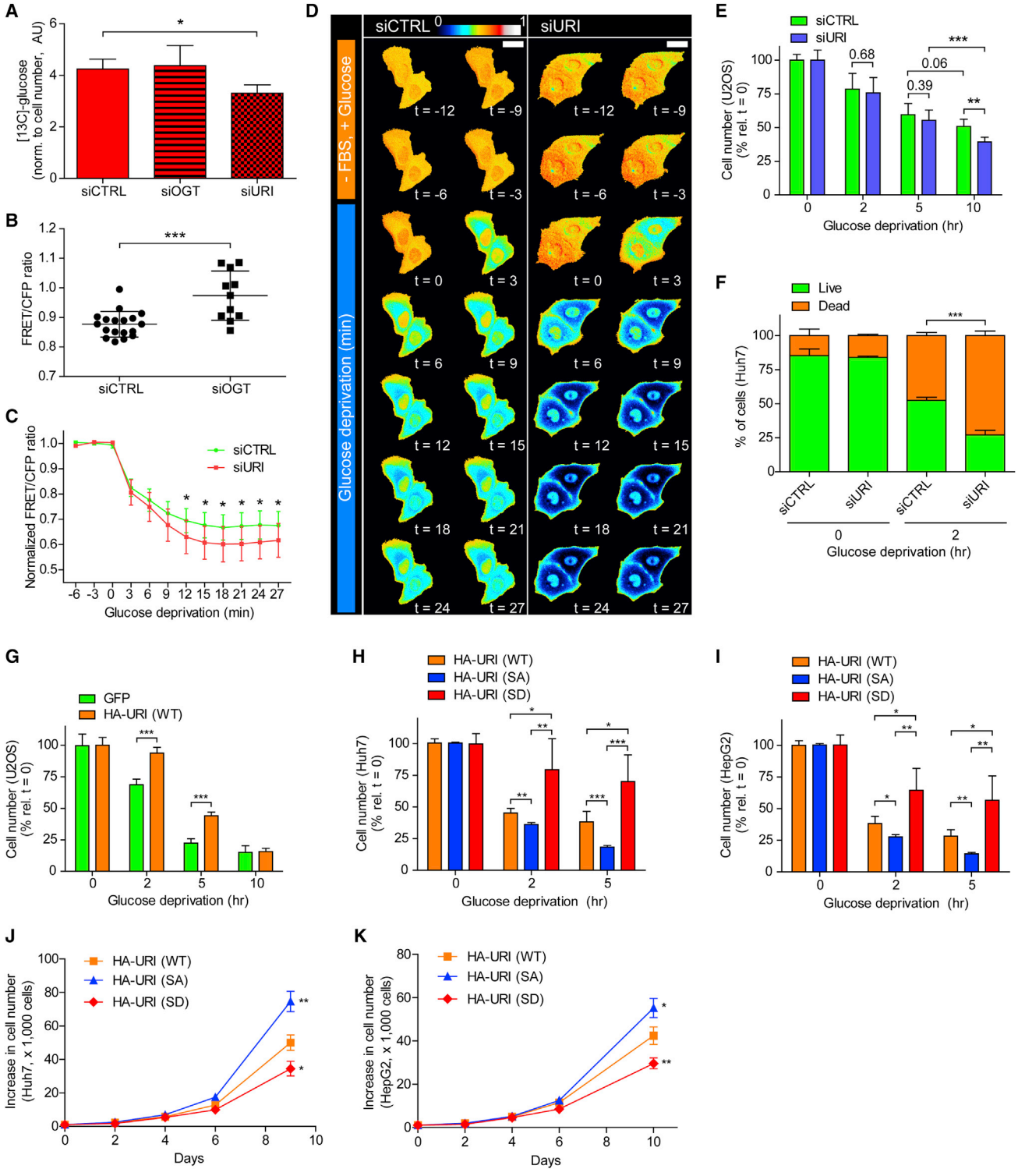

Figure 6. URI Phosphorylation at Ser-371 Protects Cancer Cells from Metabolic Stress-Induced Cell Death

(A) Intracellular ^{13}C-labeled glucose in siRNA-transfected U2OS cells upon 2 hr of glucose deprivation (Figure S4B). n = 3.

(B) Intracellular glucose, measured as FRET ratio, in siRNA-transfected U2OS cells expressing FRET glucose sensor. n = 18 (siCTRL) and n = 11 (siOGT).

(C and D) Decrease in intracellular glucose, measured as FRET ratio (C), upon glucose withdrawal in siRNA-transfected U2OS cells expressing FRET glucose sensor. n = 8 (siCTRL) and n = 15 (siURI). Scale bar, 20 μm.

(E and F) Cell number (E) and percentage of live and dead cells (F) upon glucose deprivation in siRNA-transfected U2OS (E) and Huh7 (F) cells. n = 6 (E) and n = 3 (F).

(legend continued on next page)

upon short-term glucose deprivation, while non-phosphorylated URI increases cell number when glucose is abundant.

Consistently, OGT inhibition using alloxan (Konrad et al., 2002), added upon glucose removal, increased the number of glucose-starved U2OS cells and protected Huh7 cells from apoptosis (Figures S6M and S6N). Notably, cell number or cell death in OGT-depleted cells was not affected under glucose-depleted conditions (Figures S6O and S6P), possibly due to decreased OGA levels (Figure S2A) (Zhang et al., 2014). Nevertheless, elevated O-GlcNAcylation using PUGNAC decreased their viability (Figure S6Q). Thus, URI-mediated OGT inhibition upon glucose shortage may protect cancer cells from metabolic stress-induced cell death, possibly by maintaining short-term intracellular glucose levels.

URI-Mediated O-GlcNAcylation Regulates c-MYC Protein Levels

In search of O-GlcNAcylated targets that may confer an adaptive response to glucose deprivation-induced metabolic stress, we screened by WB several known metabolic effectors. Glucose withdrawal suppressed c-MYC expression (Figures 7A and S7A). URI depletion in glucose-deprived Huh7 and U2OS cells significantly increased c-MYC levels, whereas HA-URI overexpression diminished them (Figures 7A–7C and S7B). Importantly, upon glucose deprivation, overexpression of HA-URI (S371A) in Huh7 cells increased c-MYC levels but HA-URI (S371D) decreased them when compared with HA-URI (WT) (Figures 7D, 7E, and S7C). Additionally, OGT depletion dramatically decreased c-MYC protein in various HCC cell lines (Figures 7F and S7D). Thus, c-MYC O-GlcNAcylation may be important for c-MYC stability under glucose restrictions.

Treating OGT-depleted HCC cells with MG132, a cell-permeable proteasome inhibitor, restored c-MYC levels (Figure S7E). Importantly, URI-regulated c-MYC levels depend on OGT since additional elimination of OGT in URI- and glucose-depleted Huh7 and HepG2 cells prevented c-MYC accumulation (Figures 7G and 7H). Reduced O-GlcNAcylation resulting from URI-mediated OGT inhibition may increase c-MYC degradation and provide adaptive survival responses to allow tumor cell survival under glucose restrictions.

To test this, we overexpressed c-MYC (WT) and c-MYC (T58A) in Huh7 cells. c-MYC (T58A) is a stabilized mutant since phosphorylation on its glycosylation site Thr-58, a priming step for its degradation, is prevented (Figure S7F) (Kamemura et al., 2002). Whereas under glucose deprivation URI depletion increased c-MYC (WT) levels and siRNA against OGT reduced it, no effects were observed on c-MYC (T58A) protein abundance, suggesting that phosphorylation and O-GlcNAcylation at Thr-58 are critical for c-MYC degradation and stability, respectively (Figures S7G).

Interestingly, glucose depletion induced significantly stronger phosphorylation at Ser-371 than growth factors (Figures S7H and S7I), likely due to the negative feedback loop engaged by PP1γ to restrict URI phosphorylation and S6K1 activity in the presence of growth factors (Djouder et al., 2007). We also do not exclude that other mechanisms may reduce URI phosphorylation in the presence of growth factors. Thus, URI is predominantly phosphorylated upon glucose restrictions, and OGT inhibition mainly occurs in the absence of nutrients in pathological conditions. When glucose is scarce, URI phosphorylation functions as a potent OGT inhibitor, reducing protein O-GlcNAcylation and decreasing c-MYC protein levels, which may elicit adaptive survival mechanisms for tumor cells. Conversely, when glucose is abundant, URI promotes O-GlcNAcylation and c-MYC stability, in agreement with c-MYC oncogenic functions.

Cell numbers of various cell lines overexpressing c-MYC (WT) were thus determined. In the presence of nutrients (normal growth conditions), overexpression of c-MYC (WT) increased the cell number in U2OS, Huh7, and HepG2 over time (Figures S7J–S7L), indicating that under nutrient-rich conditions, c-MYC is oncogenic. Glucose deprivation reduced the cell number in U2OS, Huh7, and HepG2, with a further decrease upon c-MYC (WT) overexpression (Figures 7I, 7J, and S7M).

Additionally, siRNA against c-MYC increased the cell number in U2OS, Huh7, and HepG2 upon glucose deprivation (Figures 7K, 7L, and S7N). In line with the fact that neither augmentation of cAMP nor URI Ser-371 phosphorylation were detected in SNU449 cells (Figures S3R and S3S), c-MYC levels appeared not important for growth of SNU449 and SNU398 cells upon glucose deprivation (Figures S7O–S7R). Furthermore, overexpressing c-MYC (WT) in these cells did not increase the cell number over time (data not shown).

Next, c-MYC (WT) or (T58A) overexpressing Huh7 and HepG2 cells were subjected to glucose deprivation in the presence or absence of URI or/and OGT (Figures 7M, S7S, and S7T). While URI depletion reduced the cell number, eliminating both URI and OGT restored the effects of URI knockdown in Huh7 and HepG2 cells overexpressing c-MYC (WT), suggesting that the protective role of URI during glucose deprivation is linked to OGT and its capacity to O-GlcNAcylate c-MYC. URI or/and OGT suppression showed almost no effect upon removal of glucose in Huh7 or HepG2 cells overexpressing c-MYC (T58A), confirming that Thr-58 is required for regulation of c-MYC upon glucose deprivation. Thus, when glucose is abundant, increased O-GlcNAcylation and, hence, c-MYC stability may accelerate tumorigenesis. In the absence of glucose, phosphorylated URI inhibits OGT, which then reduces O-GlcNAcylation and promotes c-MYC degradation, allowing cancer cell survival under pathological conditions.

Dephosphorylated URI Correlates with O-GlcNAcylation and c-MYC Levels in Human and Mouse HCC

We next explored the relationship between URI and O-GlcNAcylation in human liver tissues, by immunohistochemistry (IHC)

(G) Cell number upon glucose deprivation in U2OS cells overexpressing GFP or HA-URI (WT). n = 4.
(H and I) Cell number upon glucose deprivation in Huh7 (H) and HepG2 (I) cells overexpressing HA-URI (WT, S371A [SA], and S371D [SD]). n = 4.
(J and K) Increase in cell number of Huh7 (J) and HepG2 (K) cells overexpressing HA-URI (WT, SA, and SD), cultured in media containing 25 mM glucose and 10% FBS (nutrient-rich growth conditions). n = 3.
For (A–C) and (E–K), mean and SD error bars are shown. *p < 0.05, **p < 0.01, ***p < 0.001, unpaired t test.
See also Figure S6.

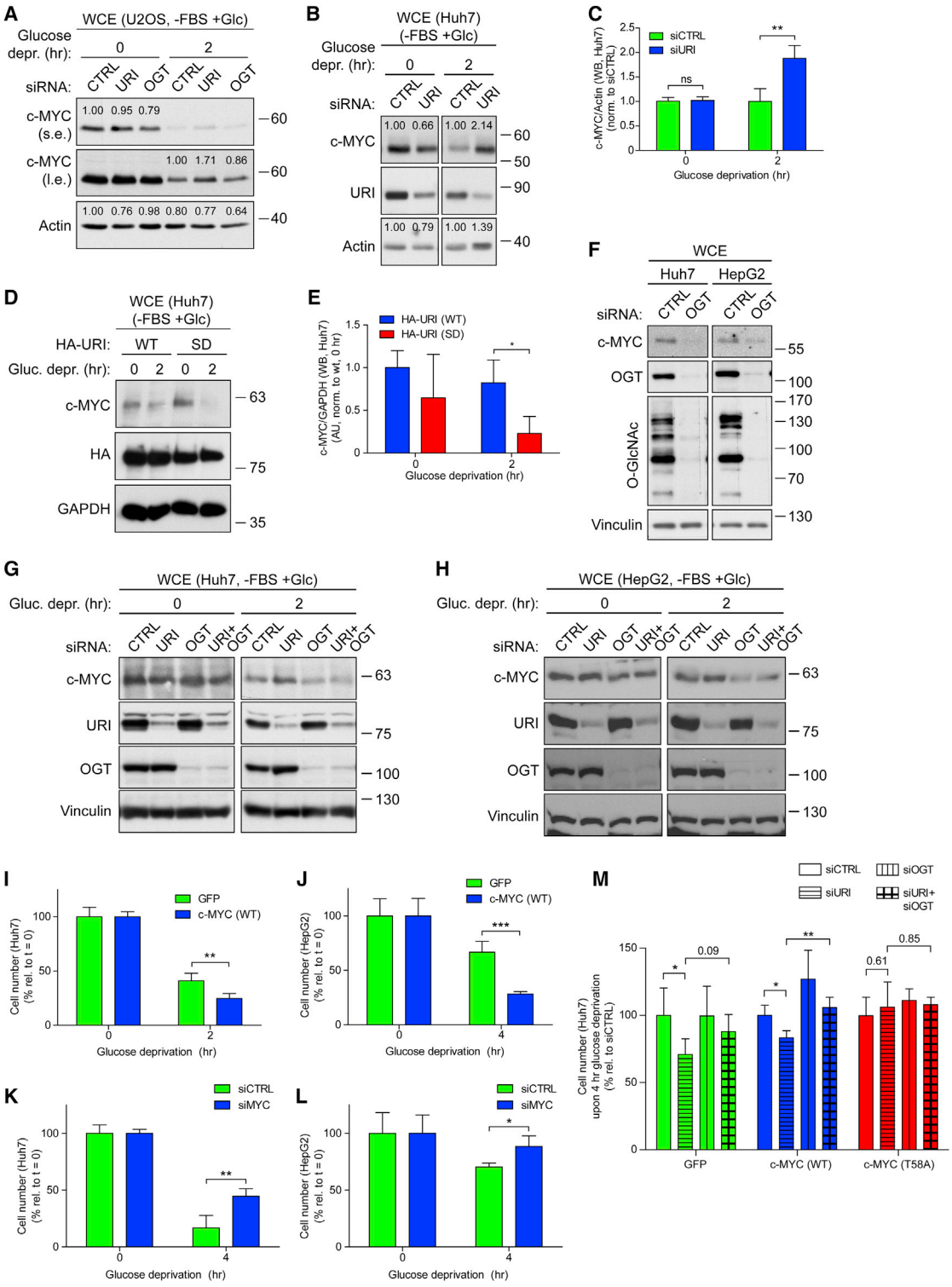

Figure 7. URI-Mediated O-GlcNAcylation Regulates c-MYC Protein Levels

(A) WB of WCE from siRNA-transfected and glucose-deprived U2OS cells. Short (s.e.) and long (l.e.) exposures are indicated.

(B and C) WB (B) and quantification (C) of c-MYC from siRNA-transfected and glucose-deprived Huh7 cells. n = 4.

(D and E) WB (D) and quantification of c-MYC (E) from HA-URI (WT and S371D [SD]) overexpressing and glucose-deprived Huh7 cells. n = 3.

(F) WB of WCE from siRNA-transfected Huh7 and HepG2 cells.

(G and H) WB of WCE from siRNA-transfected and glucose-deprived Huh7 (G) or HepG2 (H) cells.

(legend continued on next page)

using a tissue microarray (TMA) containing 44 (30 HCC, 4 peritumoral, and 10 normal) human liver samples (Tummala et al., 2014). None of the normal samples expressed URI, one peritumoral sample expressed it weakly, and 73% of the HCC samples expressed it strongly (Figure 8A). WB analysis of tumor (T)/peritumor (PT) samples exhibited differences in O-GlcNAcylation levels, and high O-GlcNAc was seen in tumors with high URI levels (Figure 8B, patients 1 and 2). In these tumors Ser-371 phosphorylation was not detected, suggesting that non-phosphorylated URI may promote O-GlcNAcylation and increase c-MYC levels, as shown by WB (Figures 8B and S8A). Paired peritumoral and tumoral samples exhibited striking differences in intracellular O-GlcNAc compartmentalization (Figures S8B–S8D). Whereas peritumor livers showed strong nuclear (and some perinuclear) O-GlcNAc, most HCC samples displayed enhanced cytoplasmic O-GlcNAc staining, possibly because the tumor cells characteristically increased glucose uptake. Importantly, the O-GlcNAc antibody's specificity in human-derived tissues was verified by IHC in HEK293T cells (Figures S8E). Human HCC tumors displaying cytoplasmic O-GlcNAcylation further stained positively for URI, but also for Ki67 and γ-H2AX (aggressive tumor and DNA damage markers, respectively), thus correlating with oncogenicity (Figures 8A, 8C, and 8D). While detection of c-MYC by IHC in HCC samples was not successful, overexpression of NES-OGT (cytoplasm-targeted) in U2OS and Huh7 cells enhanced cytoplasmic O-GlcNAcylation and c-MYC levels, supporting a causal relationship between OGT (and potentially tumorigenic cytoplasmic O-GlcNAcylation) and c-MYC (Figures S8F and S8G). Thus, URI is upregulated in human HCC, and when dephosphorylated may increase O-GlcNAcylation, c-MYC, and tumor progression.

Next, we wanted to understand why URI was dephosphorylated in human HCC samples. Using the R2 platform (http://r2.amc.nl) and Oncomine (http://www.oncomine.org/), we found that *URI* and *PP1γ* gene expression was elevated in HCC tissues, and confirmed that *URI* expression correlated with HCC progression (Figures S8H and S8I). *URI* and *PP1γ* gene expression also showed positive correlation (Figure S8J), which was further supported by WB of paired peritumoral and tumoral HCC samples (Figure 8B). By using the human HCC TMAs and comparing non-tumoral and tumoral HCC samples from 30 patients, PP1γ was upregulated in almost 60% of the tumors (Figure S8K). Its localization was almost exclusively cytoplasmic, and coincided with the absence of URI Ser-371 phosphorylation (Figure S8K). In tumors with elevated PP1γ, cytoplasmic O-GlcNAcylation was increased (Figures S8D and S8L). O-GlcNAc signals, but not URI phosphorylation, were also detected by WB in tumors with high URI and PP1γ expression (Figures 8B and S8A, patients 1 and 2). Thus, in human HCC, O-GlcNAcylation and PP1γ inversely correlated with URI phosphorylation at Ser-371, arguing that non-phosphorylated URI may increase OGT activity.

The inverse correlation between PP1γ and URI phosphorylation prompted us to test whether Ser-371 is targeted by PP1γ. PP1γ suppression in glucose-depleted U2OS cells slightly elevated Ser-371 phosphorylation (Figure S8M). Additionally, PP1γ dephosphorylated (PKA-phosphorylated) URI at Ser-371 in vitro (Figure S8N). Accordingly, HA-URI overexpression in the presence of HA-PP1γ increased O-GlcNAc levels in Huh7 cells (Figure S8O). Therefore, abundant glucose and/or high PP1γ levels promotes URI dephosphorylation and favors the trimeric complex formation, increasing O-GlcNAcylation, c-MYC stability, and hepatocarcinogenesis.

To test whether dephosphorylated URI promotes O-GlcNAcylation, increased c-MYC levels, and liver cancer, we generated a *Col1a1* knockin mouse expressing the non-phosphorylatable mutant form of human URI (S371A) (hURI (S371A)), via a tetracycline-dependent *trans*-activator controlled by the hepatocyte-specific liver-activated protein promoter (Figures S8P and S8Q). This mouse, designated hURI(S371A)tetOFF^{hep}, and littermates lacking hURI (S371A) expression, are referred to hereafter as URI(S371A)$^{(+/KI)hep}$ and URI(S371A)$^{(+/+)hep}$ mice. The mouse expressing hURI (WT) specifically in hepatocytes and named hURI(WT)tetOFF^{hep} (here URI(WT)$^{(+/+)hep}$ and URI(WT)$^{(+/KI)hep}$) was recently reported (Tummala et al., 2014).

Without doxycycline, hURI (S371A) was expressed specifically in hepatocytes (Figure S8R). Phosphorylation of URI at Ser-371 was detected in 8-week-old URI(WT)$^{(+/KI)hep}$ livers (an early time of tumorigenesis), but not in URI(S371A)$^{(+/KI)hep}$ livers (Figure 8E). WB at this age revealed increased O-GlcNAcylation and c-MYC protein abundance in URI(S371A)$^{(+/KI)hep}$ livers compared with URI(WT)$^{(+/KI)hep}$ livers (Figures 8F and 8G).

In 12-week-old livers, H&E staining revealed an increase of anisokaryotic clusters and high-grade dysplastic lesions in URI(S371A)$^{(+/KI)hep}$ livers compared with URI(WT)$^{(+/KI)hep}$ livers (Figures 8H and S8S). Increased Ki67 staining in URI(S371A)$^{(+/KI)hep}$ livers suggested that hepatocarcinogenesis may be accelerated in URI(S371A)$^{(+/KI)hep}$ mice fed with chow diet (Figures 8I and S8S). γ-H2AX was increased in 8-week-old URI(WT)$^{(+/KI)hep}$ livers (Tummala et al., 2014), and further amplified in URI(S371A)$^{(+/KI)hep}$ mice, possibly due to higher proliferation and c-MYC levels (Figures S8S and S8T).

Fibrosis in 12-week-old URI(S371A)$^{(+/KI)hep}$ livers was significantly increased compared with URI(WT)$^{(+/KI)hep}$ livers, as assessed by Sirius red and Masson trichrome staining (Figures 8J, 8K, and S8S), or by IHC and WB of α-smooth muscle actin (Figures 8F and S8S). Whereas serum alanine aminotransferase (ALT) values remained unchanged in 24-week-old URI(WT)$^{(+/KI)hep}$ mice (Tummala et al., 2014), ALT levels in URI(S371A)$^{(+/KI)hep}$ mice were significantly increased (Figure 8L), suggesting liver injury in the 24-week-old URI(S371A)$^{(+/KI)hep}$ mice.

Moreover, while no HCC were observed in URI(WT)$^{(+/KI)hep}$ livers until 32 weeks of age (Tummala et al., 2014), almost half of URI(S371A)$^{(+/KI)hep}$ livers already displayed tumors at 24 weeks

(I–L) Cell number upon glucose deprivation of Huh7 (I and K) and HepG2 (J and L) cells overexpressing GFP or His-tagged c-MYC (WT) (I and J), or transfected with siRNA (K and L). n = 4.

(M) Cell number upon glucose deprivation of Huh7 cells expressing GFP or His-tagged c-MYC (WT or T58A), additionally transfected with siRNA (Figure S7S). n = 4.

For (C), (E) and (I–M), mean and SD error bars are shown. *p < 0.05, **p < 0.01, ***p < 0.001, unpaired t test.

See also Figure S7.

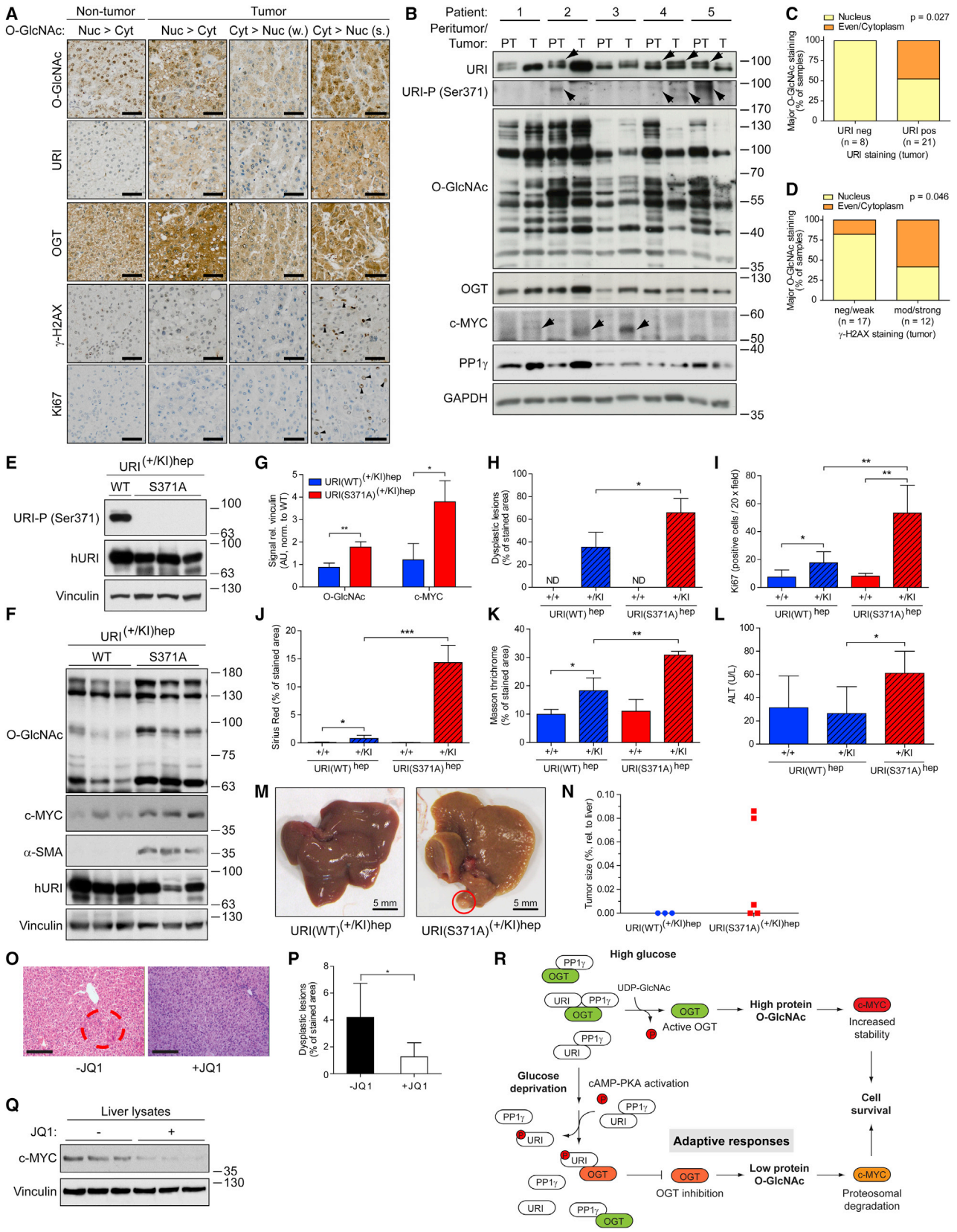

(legend on next page)

of age (Figures 8M and 8N). Accordingly, URI(WT)$^{(+/KI)hep}$ displayed increased c-MYC levels and, at a later time point, tumors with increased O-GlcNAcylation (Figures S8U and S8V). Inhibition of BET bromodomain by JQ1, known to downregulate c-MYC levels in vivo (Delmore et al., 2011), significantly reduced dysplatic lesions in 8-week-old URI(WT)$^{(+/KI)hep}$ livers (Figures 8O–8Q), consistent with the role of c-MYC in liver tumor progression (Qu et al., 2014). Therefore, dephosphorylated URI, which may result from glucose abundance and/or elevated PP1γ levels, increases O-GlcNAcylation and c-MYC stabilization and accelerates hepatocarcinogenesis (Figure 8R).

DISCUSSION

Cells growth depend on numerous factors that homeostatically regulate their metabolism and survival. Under extreme metabolic conditions, genetically unstable cancer cells undergo metabolic reprogramming and evolve sophisticated mechanisms that permit survival when nutrients are scarce. Here we show that under glucose deprivation, potentially anaplerotic reactions sustain the TCA cycle to produce energy (ATP) and provide early cellular survival adaptive responses to metabolic stress. Maintained ATP concentrations induce cAMP-dependent activation of PKA, which phosphorylates URI at Ser-371, disrupts URI/PP1γ complexes, and favors URI-mediated OGT inhibition. Lower OGT activity alters O-GlcNAc-regulated signaling pathways, enabling tumor cells to cope with glucose-mediated metabolic stress. We identify c-MYC as an OGT target and which protein levels are regulated by O-GlcNAcylation in accordance with glucose availability. In the presence of glucose, URI increases O-GlcNAcylation and promotes c-MYC-dependent oncogenesis. However, when glucose is scarce, URI reduces O-GlcNAcylation and increases c-MYC turnover to allow cells to adapt and survive under metabolic stress.

URI and c-MYC facilitate cancer cell proliferation when nutrients are abundant (Dang, 2013; Djouder et al., 2007; Soucek and Evan, 2010; Theurillat et al., 2011; Tummala et al., 2014). In glucose-deprived conditions, phosphorylated URI potently inhibits OGT, decreasing c-MYC O-GlcNAcylation and stability, thus promoting cancer cell survival. Consistently, in a colorectal cancer xenograft model, c-MYC downregulation contributes to cell survival under glucose and oxygen deficiencies (Okuyama et al., 2010). Also, high c-MYC levels are harmful to cancer cells with poor glucose supplies (Shim et al., 1998; Soucek and Evan, 2010), and URI depletion enhances O-GlcNAcylation under glucose depletion, thereby reducing c-MYC turnover, decreasing tumor cell number, and accelerating cell death. Because URI has oncogenic activities and its expression in murine hepatocytes induces spontaneous HCC (Gomes et al., 2016; Tummala et al., 2014), we demonstrate that this mechanism is relevant in hepatocarcinogenesis and that increased O-GlcNAcylation contributes to HCC by augmenting c-MYC levels. c-MYC inhibitors (e.g., JQ1) may therefore represent a therapeutic perspective in HCC treatment. Although the relevance of URI (S371D) under glucose stress conditions in hepatocarcinogenesis remains to be demonstrated, our in vitro data suggest that URI-regulated OGT and c-MYC turnover confer an adaptive survival response to glucose limitations.

URI-mediated OGT inhibition may be part of an adaptive response to maintain cellular homeostatic balance and (hence) support survival and oncogenicity during periods of metabolic stress. Like oxygen deficiency, which activates the hypoxia-inducible factor, glucose restriction assists tumor development by inducing metabolic pathway reprogramming as an adaptive response to bioenergetic stress. Sugar depletion causes cancer cells with WT KRAS alleles to acquire KRAS pathway mutations that upregulate the GLUT1 glucose transporter, enabling tumor growth under conditions lethal to normal cells (Yun et al., 2009). Oxygen and glucose are delivered to tissues via efficient microvasculature, but tumor progression often includes an early avascular stage or collapse of internal vasculature due to constriction by the surrounding cells. This compromises blood flow, reducing nutrient supply. Models for calculating nutrient diffusion coefficients in tumors suggest that oxygen and glucose restriction in nodule centers has important implications for tumor

Figure 8. Dephosphorylated URI Correlates with O-GlcNAcylation and c-MYC Levels in Human and Mouse HCC

(A) O-GlcNAc, URI, OGT, γ-H2AX, and Ki67 IHC of human liver samples from four individual patients (one non-tumor and three tumors). Tumor samples with different O-GlcNAc localization are shown. Arrows indicate cells positively stained for γ-H2AX or Ki67 in tumor with pronounced cytoplasmic O-GlcNAcylation. w., weak; s., strong. Scale bars, 50 μm.

(B) WB of peritumoral/tumoral protein lysates from five human HCC patients. Arrows indicate polypeptides cross-reacting with URI and URI Ser-371, or c-MYC, antibodies.

(C and D) Quantification of O-GlcNAc localization with URI (C) or γ-H2AX (D) staining in 29 HCC patients. p = 0.027 (C) and p = 0.046 (D). Statistical analysis was performed using Fisher's exact test.

(E–G) WB (E and F) and quantification (G) of O-GlcNAc and c-MYC in livers from 8-week-old URI(WT)$^{(+/KI)hep}$ and URI(S371A)$^{(+/KI)hep}$ mice. n = 4.

(H) Quantification of dysplastic lesions in 12-week-old livers (Figure S8S). ND, not detected. n = 4.

(I) Ki67 quantification from 12-week-old livers (Figure S8S). n = 5 (URI(WT)$^{(+/+)hep}$), n = 5 (URI(WT)$^{(+/KI)hep}$), n = 5 (URI(S371A)$^{(+/+)hep}$), and n = 4 (URI(S371A)$^{(+/KI)hep}$).

(J) Sirius red quantification from 12-week-old livers (Figure S8S). n = 5 (URI(WT)$^{(+/+)hep}$), n = 4 (URI(WT)$^{(+/KI)hep}$), n = 4 (URI(S371A)$^{(+/+)hep}$), and n = 3 (URI(S371A)$^{(+/KI)hep}$).

(K) Masson trichrome quantification from 12-week-old livers (Figure S8S). n = 4 (URI(WT)$^{(+/+)hep}$), n = 3 (URI(WT)$^{(+/KI)hep}$), n = 4 (URI(S371A)$^{(+/+)hep}$), and n = 3 (URI(S371A)$^{(+/KI)hep}$).

(L) ALT in 24-week-old mice. n = 13 (URI(WT)$^{(+/+)hep}$), n = 7 (URI(WT)$^{(+/KI)hep}$), and n = 6 (URI(S371A)$^{(+/KI)hep}$).

(M and N) Livers (M) and tumor burden quantification (N) in 24-week-old URI(WT)$^{(+/KI)hep}$ (n = 3) and URI(S371A)$^{(+/KI)hep}$ (n = 5) mice. Red circle depicts early tumor.

(O–Q) H&E (O), quantification of dysplastic lesions (P), and WB (Q) of livers from 8-week-old URI(WT)$^{(+/KI)hep}$ mice treated with JQ1. Dashed red circle depicts dysplastic area. Scale bars, 100 μm. n = 6 (URI(WT)$^{(+/KI)hep}$) and n = 4 (URI(WT)$^{(+/KI)hep}$ + JQ1).

(R) Scheme representing how URI, OGT, and PP1γ regulate c-MYC levels and cell survival in response to glucose. Active (green) and inhibited (orange) OGT are indicated. URI phosphorylated at Ser-371 is indicated with red P letter.

For (G–L) and (P), mean and SD error bars are shown. *p < 0.05, **p < 0.01, ***p < 0.001, unpaired t test.

See also Figure S8.

morphology and aggressiveness that are consistent with known effects of hypoxia in tumors (Anderson et al., 2006; Gerlee and Anderson, 2007, 2010; Pennacchietti et al., 2003). Reduction of nutrient supply favoring tumor growth may also happen during long-term nutrient-deficient diets.

Our findings suggest an important glucose-sensing mechanism in which URI acts as a rheostat controlling OGT activity and therefore c-MYC levels, conferring selective traits that allow cancer cells to tolerate severe metabolic stress and survive under selective pressures imposed by environmental challenges. This mechanism can be of general importance in tumorigenesis and may explain how cancer cells exposed to glucose deficiency can expand instead of regressing, particularly during a prolonged poor-nutrient diet or when nutrient delivery capabilities are affected through a reduced and defective vasculature. Further insights into the adaptive processes induced by glucose-restrictive conditions will clarify how glucose deprivation or excess affects clonal evolution and cancer development.

EXPERIMENTAL PROCEDURES

Materials
Materials used in this study are detailed in Supplemental Experimental Procedures.

Antibodies
We generated a specific polyclonal antibody recognizing human URI phosphorylated on Ser-371. Specificity of anti-human URI-P (Ser371) antibody was verified in HEK293T cells transiently expressing HA-URI (WT), as well as HA-URI variants. Where Thr-349 (T349A) and/or Ser-371 were point-mutated to alanine (S371A and T349A/S371A), both sites were previously shown to be phosphorylated by S6K1 (Djouder et al., 2007). Alanine-mutated HA-URI variants (S371A and T349A/S371A) were not recognized by URI-P (Ser371) antibody (Figure S3A). Antibody specificity was further confirmed in siURI-treated HeLa cell protein lysates (Figure S3B), as well as in U2OS cells treated with rapamycin (Figures S3C and S3D). These data indicate that URI-P (Ser371) antibody specifically recognizes phosphorylated URI on Ser-371.

Other antibodies used in this study are detailed in Supplemental Experimental Procedures.

siRNA and Plasmids
siRNA and plasmids used are detailed in Supplemental Experimental Procedures.

Cell Culture, Transfections, Treatments, Mitochondria Isolation, Cell Count, Cell Viability, and Colony Formation Assays
Cell culture, transfections, treatments, mitochondria isolation, cell count, cell viability, and colony formation assays were performed as detailed in Supplemental Experimental Procedures.

Immunoblots, Dot Blots, and Immunoprecipitations
Immunoblots, dot blots, and immunoprecipitations were performed as detailed in Supplemental Experimental Procedures.

Bacterial Protein Expression and Purification
Bacterial protein expression and purification were performed as detailed in Supplemental Experimental Procedures.

Size-Exclusion Chromatography
Size-exclusion chromatography was performed as detailed in Supplemental Experimental Procedures.

cAMP and ATP Measurement
cAMP and ATP levels were measured as detailed in Supplemental Experimental Procedures.

Glucose Tracing
[^{13}C]Glucose labeling and tracing was performed as detailed in Supplemental Experimental Procedures.

NMR Sample Preparation, Analysis, Spectroscopy, and Metabolite Quantification
NMR sample preparation, analysis, spectroscopy, and metabolite quantification were performed as detailed in Supplemental Experimental Procedures.

Immunofluorescence
Immunofluorescence was performed as detailed in Supplemental Experimental Procedures.

URI FRET and FRET-Based Glucose and PKA Sensors
FRET probes, with a kinase substrate module spanning the URI Ser-371 region, linker sequences, and the 14-3-3 protein's phosphoserine/threonine binding domain, was sandwiched between CFP and the cpVenus YFP variant (Figure 3B). The 14-3-3 phospho-recognition domain binds to phosphorylated Ser-371, inducing FRET via conformational changes that bring CFP and cpVenus into close proximity.

FRET assay of the URI FRET probe was performed under a confocal microscope (TCS-SP5 Leica Microsystems) using a 63 × 1.4 N.A. HCX PLAPO lens; a 458-nm laser line was used for CFP excitation collecting CFP and YFP (FRET) emission for FRET ratio calculations. Images were acquired each minute with five frames pre-stimulation and 30 frames post-stimulation (glucose deprivation).

The use of FRET-based glucose and PKA sensors are detailed in Supplemental Experimental Procedures.

In Vitro Protein Expression, GST-Binding Assays, and His-Binding Assays
In vitro protein expression, GST-binding assays, and His-binding assays were performed as detailed in Supplemental Experimental Procedures.

In Vitro Kinase, Phosphatase, and OGT Assays
In vitro kinase, phosphatase, and OGT assays were performed as described in Supplemental Experimental Procedures.

siRNA Kinase Screen
siRNA kinase screen was performed as described in Supplemental Experimental Procedures.

Histopathology and Immunohistochemistry
Histopathology and immunohistochemistry were performed as detailed in Supplemental Experimental Procedures.

Generation and Handling of Mice
hURI-tetOFF^{hep} was generated as previously described (Tummala et al., 2014). Generation and handling of hURI(S371A)tetOFF^{hep} mice is detailed in Supplemental Experimental Procedures. All experiments were approved by the CNIO-ISCIII Ethics Committee.

JQ1 Treatment
Mice were intraperitoneally injected three times per week with 50 mg/kg (+)-JQ1 (Abmole, M2167) dissolved in 5% DMSO diluted in dextrose 5% in water. Treatment started in 4-week-old mice that were euthanized and analyzed at 8 weeks of age.

Human Samples
Human samples were obtained from the histopathology files of UCL Hospital, from patients after approval by the Institutional Research Ethics Committee (Central London REC 3, Reference 06/Q0512/106), and CNIO Biobank. Informed consent was obtained from all subjects.

Statistical Analysis
Statistical analyses were performed using GraphPad Prism 5. Statistical significance (*$p < 0.05$, **$p < 0.01$, ***$p < 0.001$) between the means of a minimum of three groups was determined using an unpaired two-tailed Student's

t test, and results are presented as the mean value and SD unless stated otherwise.

SUPPLEMENTAL INFORMATION

Supplemental Information includes Supplemental Experimental Procedures and eight figures and can be found with this article online at http://dx.doi.org/10.1016/j.ccell.2016.06.023.

AUTHOR CONTRIBUTIONS

S.B. and N.D. designed the project and experiments. S.B. performed most experiments. A.T. performed all experiments with the hURI-tetOFF^{hep} mice. A.G. and R.C.O. performed and analyzed NMR experiments. M.A. performed size-exclusion chromatography and some cell counting. K.S.T. and N.D. engineered the hURI(WT)-tetOFF^{hep} and the hURI(S371A)-tetOFF^{hep} mouse, together with M.Y. M.P. and D.M. performed and analyzed confocal microscopy experiments. M.R.J. assessed histologically the human samples as previously reported (Tummala et al., 2014). S.B. and N.D. analyzed all the data. N.D. wrote the manuscript with S.B. N.D. designed the study and secured all funding.

ACKNOWLEDGMENTS

We thank G. Hart, E. B. Affar, X. Yu, L. Wells and J. Zhang for sharing reagents. We thank the CNIO Biobank for collecting human samples. We thank M. Bylesjö for helping with statistics, B. López-Méndez for technical help on NMR sample preparation and J. Soriano for some microscopy analysis. We thank L. Bakiri, G. Montoya, R. Ricci and E. Wagner for critical reading of the manuscript and, W. Krek for fruitful scientific discussions. N.D. is a recipient of the Spanish Ramón y Cajal fellowship. This work was supported by the Spanish Ministry of Economy and Competitiveness (SAF2010-18518 and SAF2013-46089-R) and WCR (AICR-UK 11-0242). The authors declare no conflict of interest.

Received: December 18, 2014
Revised: August 1, 2015
Accepted: June 29, 2016
Published: August 8, 2016

REFERENCES

Allen, M.D., and Zhang, J. (2006). Subcellular dynamics of protein kinase A activity visualized by FRET-based reporters. Biochem. Biophys. Res. Commun. *348*, 716–721.

Anderson, A.R., Weaver, A.M., Cummings, P.T., and Quaranta, V. (2006). Tumor morphology and phenotypic evolution driven by selective pressure from the microenvironment. Cell *127*, 905–915.

Bollen, M., Peti, W., Ragusa, M.J., and Beullens, M. (2010). The extended PP1 toolkit: designed to create specificity. Trends Biochem. Sci. *35*, 450–458.

Caldwell, S.A., Jackson, S.R., Shahriari, K.S., Lynch, T.P., Sethi, G., Walker, S., Vosseller, K., and Reginato, M.J. (2010). Nutrient sensor O-GlcNAc transferase regulates breast cancer tumorigenesis through targeting of the oncogenic transcription factor FoxM1. Oncogene *29*, 2831–2842.

Dang, C.V. (2013). MYC, metabolism, cell growth, and tumorigenesis. Cold Spring Harb. Perspect. Med. *3*, http://dx.doi.org/10.1101/cshperspect.a014217.

Danial, N.N., Gramm, C.F., Scorrano, L., Zhang, C.Y., Krauss, S., Ranger, A.M., Datta, S.R., Greenberg, M.E., Licklider, L.J., Lowell, B.B., et al. (2003). BAD and glucokinase reside in a mitochondrial complex that integrates glycolysis and apoptosis. Nature *424*, 952–956.

Delmore, J.E., Issa, G.C., Lemieux, M.E., Rahl, P.B., Shi, J., Jacobs, H.M., Kastritis, E., Gilpatrick, T., Paranal, R.M., Qi, J., et al. (2011). BET bromodomain inhibition as a therapeutic strategy to target c-Myc. Cell *146*, 904–917.

Djouder, N., Metzler, S.C., Schmidt, A., Wirbelauer, C., Gstaiger, M., Aebersold, R., Hess, D., and Krek, W. (2007). S6K1-mediated disassembly of mitochondrial URI/PP1gamma complexes activates a negative feedback program that counters S6K1 survival signaling. Mol. Cell *28*, 28–40.

Doege, K., Heine, S., Jensen, I., Jelkmann, W., and Metzen, E. (2005). Inhibition of mitochondrial respiration elevates oxygen concentration but leaves regulation of hypoxia-inducible factor (HIF) intact. Blood *106*, 2311–2317.

Ferrer, C.M., Lynch, T.P., Sodi, V.L., Falcone, J.N., Schwab, L.P., Peacock, D.L., Vocadlo, D.J., Seagroves, T.N., and Reginato, M.J. (2014). O-GlcNAcylation regulates cancer metabolism and survival stress signaling via regulation of the HIF-1 pathway. Mol. Cell *54*, 820–831.

Gerlee, P., and Anderson, A.R. (2007). An evolutionary hybrid cellular automaton model of solid tumour growth. J. Theor. Biol. *246*, 583–603.

Gerlee, P., and Anderson, A.R. (2010). Diffusion-limited tumour growth: simulations and analysis. Math. Biosci. Eng. *7*, 385–400.

Gibbons, J.A., Weiser, D.C., and Shenolikar, S. (2005). Importance of a surface hydrophobic pocket on protein phosphatase-1 catalytic subunit in recognizing cellular regulators. J. Biol. Chem. *280*, 15903–15911.

Gomes, A., Teijeiro, A., Buren, S., Tummala, K., Yilmaz, M., Waisman, A., Theurilat, J.P., Perna, C., and Djouder, N. (2016). Metabolic Inflammation-Associated IL-17A Causes Non-alcoholic Steatohepatitis and Hepatocellular Carcinoma. Cancer Cell *30*, 161–175.

Griffith, L.S., and Schmitz, B. (1999). O-linked N-acetylglucosamine levels in cerebellar neurons respond reciprocally to pertubations of phosphorylation. Eur. J. Biochem. *262*, 824–831.

Hardiville, S., and Hart, G.W. (2014). Nutrient regulation of signaling, transcription, and cell physiology by O-GlcNAcylation. Cell Metab. *20*, 208–213.

Hart, G.W., and Akimoto, Y. (2009). The O-GlcNAc modification. In Essentials of Glycobiology, A. Varki, R.D. Cummings, J.D. Esko, H.H. Freeze, P. Stanley, C.R. Bertozzi, G.W. Hart, and M.E. Etzler, eds. (Cold Spring Harbor, NY: Cold Spring Harbor Laboratory Press), Chapter 18.

Kamemura, K., Hayes, B.K., Comer, F.I., and Hart, G.W. (2002). Dynamic interplay between O-glycosylation and O-phosphorylation of nucleocytoplasmic proteins: alternative glycosylation/phosphorylation of THR-58, a known mutational hot spot of c-Myc in lymphomas, is regulated by mitogens. J. Biol. Chem. *277*, 19229–19235.

Konrad, R.J., Zhang, F., Hale, J.E., Knierman, M.D., Becker, G.W., and Kudlow, J.E. (2002). Alloxan is an inhibitor of the enzyme O-linked N-acetylglucosamine transferase. Biochem. Biophys. Res. Commun. *293*, 207–212.

Lazarus, M.B., Nam, Y., Jiang, J., Sliz, P., and Walker, S. (2011). Structure of human O-GlcNAc transferase and its complex with a peptide substrate. Nature *469*, 564–567.

Love, D.C., Kochan, J., Cathey, R.L., Shin, S.H., and Hanover, J.A. (2003). Mitochondrial and nucleocytoplasmic targeting of O-linked GlcNAc transferase. J. Cell Sci. *116*, 647–654.

Ma, Z., and Vosseller, K. (2014). Cancer metabolism and elevated O-GlcNAc in oncogenic signaling. J. Biol. Chem. *289*, 34457–34465.

Ma, L., Tao, Y., Duran, A., Llado, V., Galvez, A., Barger, J.F., Castilla, E.A., Chen, J., Yajima, T., Porollo, A., et al. (2013). Control of nutrient stress-induced metabolic reprogramming by PKCzeta in tumorigenesis. Cell *152*, 599–611.

Okuyama, H., Endo, H., Akashika, T., Kato, K., and Inoue, M. (2010). Downregulation of c-MYC protein levels contributes to cancer cell survival under dual deficiency of oxygen and glucose. Cancer Res. *70*, 10213–10223.

Pathak, S., Borodkin, V.S., Albarbarawi, O., Campbell, D.G., Ibrahim, A., and van Aalten, D.M. (2012). O-GlcNAcylation of TAB1 modulates TAK1-mediated cytokine release. EMBO J. *31*, 1394–1404.

Pennacchietti, S., Michieli, P., Galluzzo, M., Mazzone, M., Giordano, S., and Comoglio, P.M. (2003). Hypoxia promotes invasive growth by transcriptional activation of the met protooncogene. Cancer Cell *3*, 347–361.

Qu, A., Jiang, C., Cai, Y., Kim, J.H., Tanaka, N., Ward, J.M., Shah, Y.M., and Gonzalez, F.J. (2014). Role of Myc in hepatocellular proliferation and hepatocarcinogenesis. J. Hepatol. *60*, 331–338.

Shim, H., Chun, Y.S., Lewis, B.C., and Dang, C.V. (1998). A unique glucose-dependent apoptotic pathway induced by c-Myc. Proc. Natl. Acad. Sci. USA *95*, 1511–1516.

Slawson, C., Copeland, R.J., and Hart, G.W. (2010). O-GlcNAc signaling: a metabolic link between diabetes and cancer? Trends Biochem. Sci. *35*, 547–555.

Soucek, L., and Evan, G.I. (2010). The ups and downs of Myc biology. Curr. Opin. Genet. Dev. *20*, 91–95.

Takanaga, H., Chaudhuri, B., and Frommer, W.B. (2008). GLUT1 and GLUT9 as major contributors to glucose influx in HepG2 cells identified by a high sensitivity intramolecular FRET glucose sensor. Biochim. Biophys. Acta *1778*, 1091–1099.

Theurillat, J.P., Metzler, S.C., Henzi, N., Djouder, N., Helbling, M., Zimmermann, A.K., Jacob, F., Soltermann, A., Caduff, R., Heinzelmann-Schwarz, V., et al. (2011). URI is an oncogene amplified in ovarian cancer cells and is required for their survival. Cancer Cell *19*, 317–332.

Tummala, K.S., Gomes, A.L., Yilmaz, M., Grana, O., Bakiri, L., Ruppen, I., Ximenez-Embun, P., Sheshappanavar, V., Rodriguez-Justo, M., Pisano, D.G., et al. (2014). Inhibition of de novo NAD(+) synthesis by oncogenic URI causes liver tumorigenesis through DNA damage. Cancer Cell *26*, 826–839.

Wells, L., Kreppel, L.K., Comer, F.I., Wadzinski, B.E., and Hart, G.W. (2004). O-GlcNAc transferase is in a functional complex with protein phosphatase 1 catalytic subunits. J. Biol. Chem. *279*, 38466–38470.

Wick, A.N., Drury, D.R., Nakada, H.I., and Wolfe, J.B. (1957). Localization of the primary metabolic block produced by 2-deoxyglucose. J. Biol. Chem. *224*, 963–969.

Yun, J., Rago, C., Cheong, I., Pagliarini, R., Angenendt, P., Rajagopalan, H., Schmidt, K., Willson, J.K., Markowitz, S., Zhou, S., et al. (2009). Glucose deprivation contributes to the development of KRAS pathway mutations in tumor cells. Science *325*, 1555–1559.

Zhang, Z., Tan, E.P., VandenHull, N.J., Peterson, K.R., and Slawson, C. (2014). O-GlcNAcase expression is sensitive to changes in O-GlcNAc homeostasis. Front Endocrinol. *5*, 206.

Zhu, Q., Zhou, L., Yang, Z., Lai, M., Xie, H., Wu, L., Xing, C., Zhang, F., and Zheng, S. (2012). O-GlcNAcylation plays a role in tumor recurrence of hepatocellular carcinoma following liver transplantation. Med. Oncol. *29*, 985–993.

Zhu, G., Tao, T., Zhang, D., Liu, X., Qiu, H., Han, L., Xu, Z., Xiao, Y., Cheng, C., and Shen, A. (2016). O-GlcNAcylation of histone deacetylases 1 in hepatocellular carcinoma promotes cancer progression. Glycobiology, 1–14, http://dx.doi.org/10.1093/glycob/cww025.